Chemical Science

MINIREVIEW

View Article Online
View Journal | View Issue

Check for updates

Cite this: *Chem. Sci.*, 2018, **9**, 7727

All publication charges for this article have been paid for by the Royal Society of Chemistry

Received 13th June 2018
Accepted 23rd September 2018

DOI: 10.1039/c8sc02609b

rsc.li/chemical-science

Open Access Article. Published on 24 September 2018. Downloaded on 10/19/2018 10:38:30 AM.
This article is licensed under a Creative Commons Attribution-NonCommercial 3.0 Unported Licence.

Charge carrier injection and transport engineering in two-dimensional transition metal dichalcogenides

José Ramón Durán Retamal, Dharmaraj Periyanagounder, Jr-Jian Ke, Meng-Lin Tsai and Jr-Hau He *

Computer, Electrical and Mathematical Sciences and Engineering, King Abdullah University of Science and Technology, Thuwal, 23955-6900, Kingdom of Saudi Arabia. E-mail: jrhau.he@kaust.edu.sa

Ever since two dimensional-transition (2D) metal dichalcogenides (TMDs) were discovered, their fascinating electronic properties have attracted a great deal of attention for harnessing them as critical components in novel electronic devices. 2D-TMDs endowed with an atomically thin structure, dangling bond-free nature, electrostatic integrity, and tunable wide band gaps enable low power consumption, low leakage, ambipolar transport, high mobility, superconductivity, robustness against short channel effects and tunneling in highly scaled devices. However, the progress of 2D-TMDs has been hampered by severe charge transport issues arising from undesired phenomena occurring at the surfaces and interfaces. Therefore, this review provides three distinct engineering strategies embodied with distinct innovative approaches to optimize both carrier injection and transport. First, contact engineering involves 2D-metal contacts and tunneling interlayers to overcome metal-induced interface states and the Fermi level pinning effect caused by low vacancy energy formation. Second, dielectric engineering covers high-*k* dielectrics, ionic liquids or 2D-insulators to screen scattering centers caused by carrier traps, imperfections and rough substrates, to finely tune the Fermi level across the band gap, and to provide dangling bond-free media. Third, material engineering focuses on charge transfer *via* substitutional, chemical and plasma doping to precisely modulate the carrier concentration and to passivate defects while preserving material integrity. Finally, we provide an outlook of the conceptual and technical achievements in 2D-TMDs to give a prospective view of the future development of highly scaled nanoelectronic devices.

1. Introduction

Since Moore's law was proposed in 1965 and with the advance of conventional Si technology, the semiconductor industry has

José Ramón Durán Retamal received his B.S. (2007) from the Telecommunication Engineering School, Technical University of Madrid, M.S. (2010) from Electrical Engineering Department and Ph.D. (2014) from the Graduate Institute of Photonics and Optoelectronics at the National Taiwan University. Currently, he is a postdoctoral fellow at the Computer, Electrical and Mathematical Sciences and Engineering Division of King Abdullah University of Science and Technology (KAUST). His past research activities include metal oxide nanostructure based electronic devices including transistors, photodetectors, and memories. More recently, his research focuses on elucidating and improving the carrier transport through 2D-TMD lateral heterojunctions.

Dharmaraj Periyanagounder is working as a visiting student in the Electrical Engineering Department at the Computer, Electrical and Mathematical Sciences and Engineering (CEMSE) Division of the King Abdullah University of Science and Technology (KAUST). Dharma's research interests are the device physics of 2D materials and their heterostructures for technologically useful electronic, optoelectronic and thermoelectric applications. He is now extensively involved in the micro/nanofabrication of 2D material-based devices by high resolution e-beam lithography.

Open Access Article. Published on 24 September 2018. Downloaded on 10/19/2018 10:38:30 AM.
This article is licensed under a Creative Commons Attribution-NonCommercial 3.0 Unported Licence.

been consistently and prosperously developed over the past half-century. However, as Si technology is approaching the fundamental size scaling limit in the sub 10 nm regime, the material roughness and the short channel effects (SCEs) dominate the carrier transport, which could infer the end of Moore's law. Moreover, it is crucial to reduce the power consumption without sacrificing device performance.[1,2] Indeed, there exists a theoretical Boltzmann limit for subthreshold swing (SS, the figure-of-merit that determines the switching characteristics of FETs) of 60 mV dec^{-1} at 300 K that can be overcome by tunneling transistors and negative capacitance transistors.[3–6] Therefore, the major challenge of the semiconductor industry in the following years is to find novel sub-nanometer materials and transistor geometries that enable high performance and low power consumption devices. Toward this challenge, the superior electronic properties including the excellent electrostatic integrity, tunable bandgaps, high electron/hole mobility, and gate-tunable superconductivity of novel two dimensional-transition metal dichalcogenides (2D-TMDs) have enabled the development of nanoscale devices with exceptional transport properties, thus holding promise for the next-generation of semiconductor materials towards their applicability in diverse applications such as transistors, digital circuits, optoelectronic systems and chemical sensors.[7–15] As charge carriers are strongly confined in atomically thin layers, the critical issues associated with SCEs can be completely eliminated, thereby broadening the range of applications toward highly energy efficient devices.[12,16,17] Furthermore, the gate controllable atomically thin TMD channel enables a high electric field at the tunnel junction to strongly increase the on-current and to reduce the subthermionic SS down to 3.9 mV dec^{-1}, which provides a significant breakthrough for applications in the future semiconductor industry.[18,19]

Despite the growing interest in 2D-TMD materials, there are several bottlenecks that block the progress as well as the integration of TMDs with modern semiconductor technology.[20–22] Specifically, and as prescribed by the international technology roadmap for semiconductors (ITRS), the primary step toward highly efficient electronic devices is that the metal electrode/TMD contact resistance (R_C) should be as low as ~100 Ω μm.[23] This is not the case for most 2D-TMD based devices fabricated so far due to their detrimental interface states.[22,24] In addition, owing to the nature of the metal/TMD chemical bond, the contact geometry plays a key role in determining R_C. On the other hand, the carrier transport efficiency, mainly limited by carrier traps and phonon-scattering centers, can be notoriously affected by impurities or imperfections along the channel owing to the high surface-to-volume ratio of 2D-TMDs, hence becoming a cornerstone toward high mobility devices.[25–31] In this regard, strategies engineering the surrounding gate dielectric as well as functionalizing the surface play a starring role in boosting the performance.[20,32] Consequently, it is of paramount importance to deeply scrutinize not only the fundamental limitations of the current transport but also the strategies to overcome such limitations in order to precisely control the electronic properties of 2D-TMDs toward high

Jr-Jian Ke received his B.S. (2007) in electrical engineering from the National University of Kaohsiung, Kaohsiung, Taiwan, and his M.S. (2009) and Ph. D (2016) degrees from the Graduate Institute of Photonics and Optoelectronics, National Taiwan University, Taipei, Taiwan. His past research activities include the transport mechanism of nanowires and metal–semiconductor interfaces. He is now working on the fabrication and transport modeling of resistive random-access memory devices and their applications.

Meng-Lin Tsai received his B.S. degree from National Tsing Hua University, Hsinchu, Taiwan. He is currently with the Department of Electrical Engineering, and the Graduate Institute of Photonics and Optoelectronics, National Taiwan University, Taipei, Taiwan. Currently, he is working at Taiwan Semiconductor Manufacturing Company (TSMC).

Dr. Jr-Hau He is an Associate Professor of Electrical Engineering program at King Abdullah University of Science & Technology (KAUST). His breakthrough research in 2D materials/electronics and photoelectrochemical water splitting has been highlighted over 50 times by various scientific magazines such as Nature, Nature Materials, IEEE SPECTRUM, EE Times, Semiconductor Today, Materials Today, Chemical & Engineering News, and Nano Today. He participates actively in activities and services in scientific professional societies. He is a Fellow of RSC and SPIE, and a senior member of IEEE and OSA.

This journal is © The Royal Society of Chemistry 2018

Open Access Article. Published on 24 September 2018. Downloaded on 10/19/2018 10:38:30 AM.
This article is licensed under a Creative Commons Attribution-NonCommercial 3.0 Unported Licence.

performance electronic devices beyond scaling and physical limits.

Accordingly, we summarize recent advances and challenges encountered in the development of 2D-TMD based electronic devices. First, we provide insight on factors influencing the carrier injection such as the Fermi level pinning (FLP) or the Schottky barrier (SB), and accordingly how to precisely estimate R_C. Second, based on the scattering limited mobility edge concept, we discern the current transport mechanism along the channel and emphasize the carrier-density-dependent metal-to-insulator (MIT) transition as well as the ballistic transport of highly scaled devices. Third, we review how several strategies involving surface and interface chemistry can synergistically improve both carrier injection and current transport, highlighting the importance of doping and phase transformation. Finally, we provide an outlook of the major achievements and give a perspective of future research directions for developing high performance 2D-TMD based electronic devices.

2. Contact resistance and current transport in 2D-TMDs

To discuss the electronic properties of 2D-TMDs, we first discuss the theoretical framework, current transport mechanism and experimental accuracy to understand how the processability, low dimensionality and novel properties of 2D-TMDs limit the carrier injection due to high contact resistance and deviate the ideal phonon-limited mobility carrier transport due to scattering centers and imperfections in real devices with highly scaled dimensional features.

2.1. Metal/TMD contact and the Fermi level pinning effect

The metal/semiconductor (M/S) contact is one of the most critical aspects of electronic transport that explicitly determines the device performance such as contact resistance, carrier mobility, switching speed, on-state current, and so forth. Typically, the energy misalignment between the metal work function (ϕ_M) and the semiconductor electron affinity (χ) leads to a Schottky barrier height (SBH) at the M/S interface, $\phi_B = \phi_M - \chi$, that determines whether the contact resistance is either high and non-linear or low and linear. In this regard, Fig. 1a shows the band alignment between the semiconducting bandgaps (electron affinity and ionization potential) of 2D-TMDs and the work functions of commonly used metals.[33] However, the electrostatic potential originated by the SBH can be modulated by metal-induced interface states within the semiconductor bandgap during the metal deposition, pinning the semiconductor Fermi level toward the charge neutrality level (ϕ_{CNL}), and thus inducing a SBH displacement expressed as $\phi_B = S(\phi_M - \phi_{CNL}) + (\phi_{CNL} - \chi) = S\phi_M + b$, where $S = d\phi_B/d\phi_M$ is the pinning factor indicating strong ($S = 0$) or weak ($S = 1$) FLP, and b is the energy above which the states of a neutral surface are empty; accordingly, $\phi_B = (\chi + b)/(1 - S)$.[22,24,31] Therefore, the FLP effect dominates the charge injection at the M/S interface and

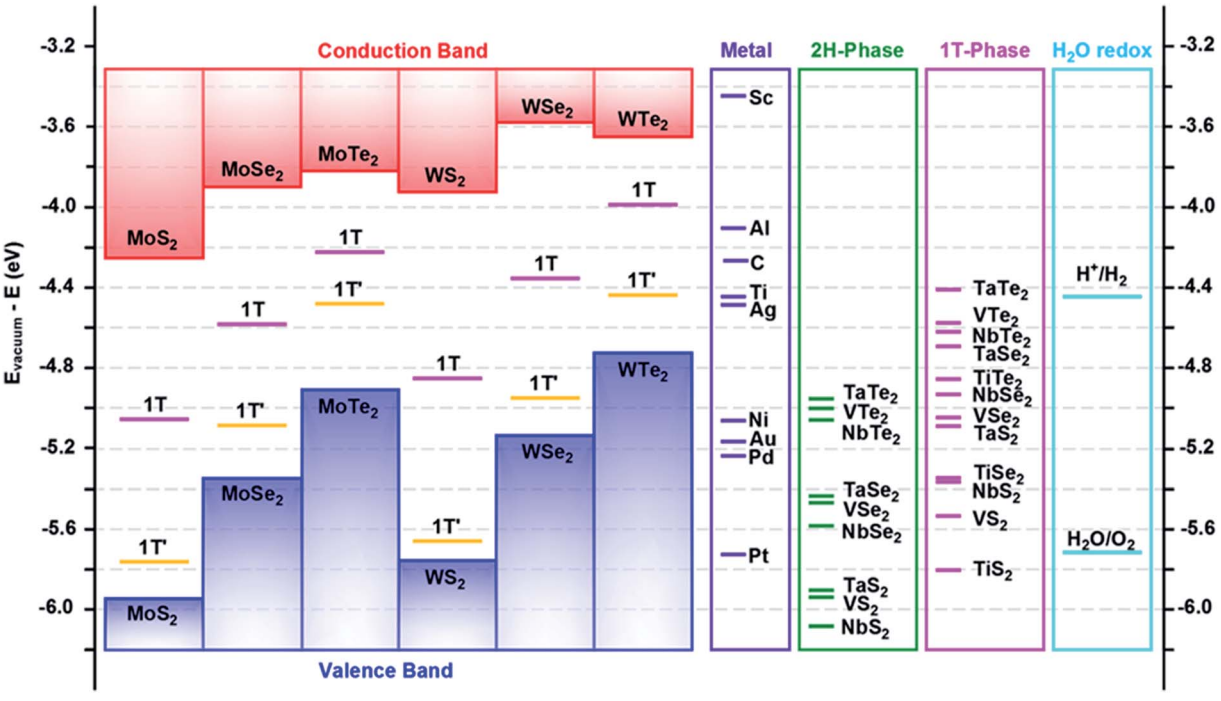

Fig. 1 2H-semiconducting bandgaps (electron affinity and ionization potential) and 1T and 1T′ metallic phase work functions (dashed orange lines). Band alignment between the electron affinity and ionization potential of 2H-semiconducting MX_2 (M: W, Mo; X: S, Se, and Te) TMDs and the work function of materials with metallic behavior: 1T- and 1T′-phases of MX_2 (M: W, Mo; X: S, Se, and Te), conventional metals, C: pristine graphene, and 2H- and 1T-phases of 2D-metals MX_2 (M: Ta, V, Nb, and Ti; X: S, Se, and Te). The water redox reaction potentials are also shown for comparison with surface charge transfer by chemical dopants.[33,172] Reproduced with permission from ref. 33 copyright© 2016 American Association for the Advancement of Science.

Open Access Article. Published on 24 September 2018. Downloaded on 10/19/2018 10:38:30 AM.
This article is licensed under a Creative Commons Attribution-NonCommercial 3.0 Unported Licence.

effectively modulates the SBH regardless of ϕ_M, which suggests metal work function independent R_C.

Indeed, several groups have reported that the low sulfur vacancy formation energy (1.6 eV) of MoS_2 induces strong FLP regardless of the metal contact.[24,34] Nevertheless, the FLP effect on MoS_2 has evoked a great deal of discrepancy. For instance, if we only consider solely the difference between the MoS_2 electron affinity and the metal work functions of Sc, Ti, Ni, and Pt, which spans from 3.5 to 5.9 eV (Fig. 2a), the corresponding transfer characteristics should look like Fig. 2b; however, experimental results show n-type behavior for all metals, indicating that the Fermi levels line-up close to the conduction band edge of MoS_2 (Fig. 2c).[23] Further simulations and experiments indicate that the FLP is dictated by the synergy between metal work function modification caused by the dipole formation and the presence of a high density of interface gap states caused by chalcogenide-mediated hybridization.[23,35–38] Conversely, theoretical calculations show that low (high) work function metals exhibit strong (weak) FLP due to the high density of interface states.[39] To solve the discrepancy, one can depict as a figure-of-merit the theoretical and experimental SBH *versus* several metal work functions and calculate the pinning factor; if the pinning factors are significantly lower than theoretical predictions, the SBH does not follow the Schottky–Mott rule, as is the case of MoS_2 (Fig. 2d and e) and $MoTe_2$.[24] However, the chemical disorder and FLP induced by high-energy metal deposition on MoS_2 can be overcome by transferring metal electrodes, and thus form flawless van der Waals (vdW) M/S interfaces which follow the Schottky–Mott rule (see Section 3.1 and 3.2 for further details).[40] On the other hand, all the other 2D-TMDs do not exhibit the FLP effect but rather exhibit ambipolar carrier transport due to the line up of their large vacancy formation energies near the mid-gap.[34] Furthermore, although the thickness scaling effect leads to band gap increases with decreasing number of layers due to the quantum confinement, the pinning position between monolayer and few layer MoS_2 remains roughly constant, revealing strong FLP; consequently, the SBH increases with decreasing layer thickness, and thus the contact resistance greatly enhances at the monolayer limit (Fig. 2f).[10,41]

2.2. Contact resistance estimation

Typically, the dangling bond-free nature of 2D-TMDs should not lead to the formation of any chemical bond with metals, and thus increase the risk of high contact resistances (R_C). Nevertheless, the R_C values reported so far range from hundreds to millions of Ω μm depending on the contact approach and the degree of accuracy of the selected method to estimate R_C as we next discuss.[42] (i) Two-probe measurement assumes solely thermionic emission with a given SBH ≤ 0.1 eV to evaluate $R_C = (h^3/4\pi e^2 m^* t k_B T)\exp(q\phi_B/k_B T)$, where h, k_B, m^*, and t are Planck's constant, Boltzmann constant, effective mass, and thickness, respectively.[43] (ii) Two-probe FET measurements extract R_C by polynomial fitting $b1 + b2/x + b3/x^2$ of the total resistance (R_T) *vs.* V_{gs} as $2R_C = b1$.[44] (iii) The transmission line model (TLM) based on a series of TMDs and two back-to-back contacts estimates R_C from $R_T = 2R_C + R_i$, where R_i is the TMD resistance. When the current flows across the metal/TMD junction, a resistor ladder network composed of the sheet resistance R_{sh} and the SB-

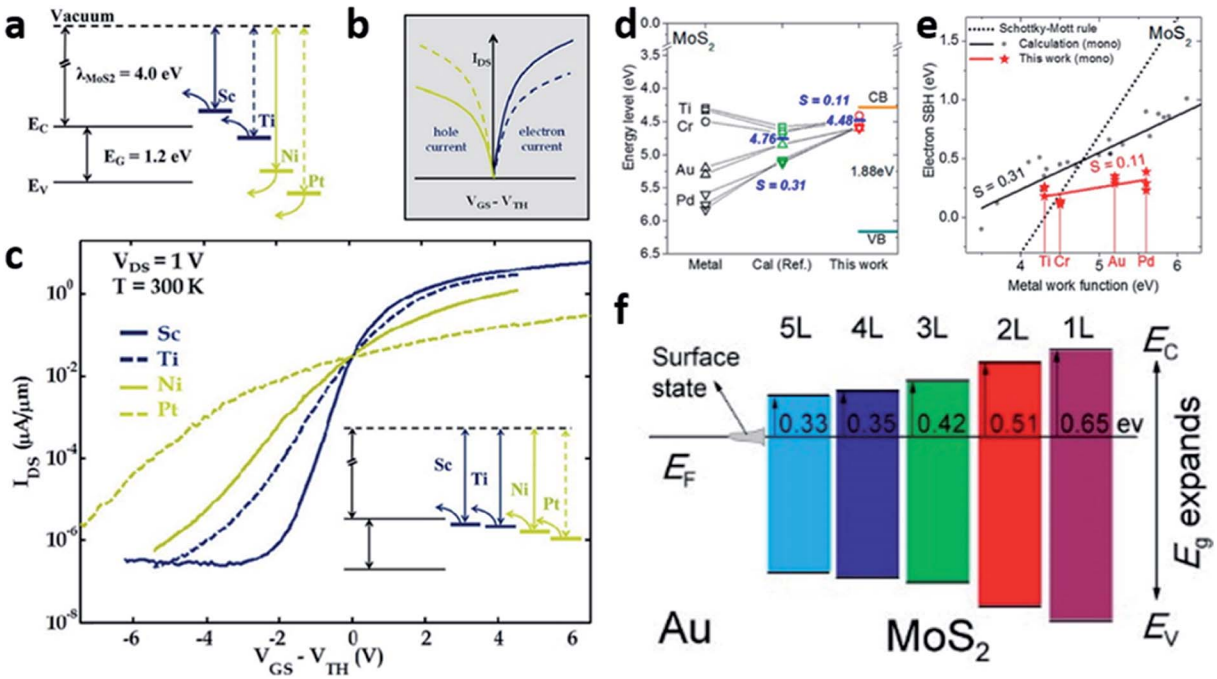

Fig. 2 (a) Expected band structure as the Sc, Ti, Ni and Pt work functions line up with the electronic band of MoS_2. (b) Theoretical and (c) experimental transfer characteristics based on (a).[23] Fermi level pinning (d) effect and (e) S factors of monolayer MoS_2 with respect to theoretical and experimental SBH *vs.* metal work function (Ti, Cr, Au, and Pd), and Schottky–Mott rule prediction.[24] Energy band alignment evolution between Au and one to five layer MoS_2.[41] Reproduced with permission from ref. 23 copyright© 2013 American Chemical Society; ref. 24 copyright© 2017 American Chemical Society; ref. 41 copyright© 2014 American Chemical Society.

 This journal is © The Royal Society of Chemistry 2018

Open Access Article. Published on 24 September 2018. Downloaded on 10/19/2018 10:38:30 AM.
This article is licensed under a Creative Commons Attribution-NonCommercial 3.0 Unported Licence.

induced specific contact resistivity ρ_c leads to $R_C = (R_{sh}L_T/W)\coth(L/L_T)$, where L is the contact length and $L_T = \sqrt{\rho_C/R_{sh}}$ is the effective contact transfer length for the carrier injection, a parameter that describes the distance over which $1/e$ of the current is transferred to the metal contact (Fig. 3).[45–47] For short L_T, the current crosses around the contact edge, while for long L_T, the current involves larger contact areas.[45] This current injection phenomenon, termed as current crowding, imposes device scaling limits because if $L < L_T$, R_C increases abruptly.[48,49] Therefore, keeping $L \gg 1.5\,L_T$ is crucial to avoid high R_C and to keep L-independent R_C when downscaling devices; consequently, $\coth(L/L_T) \sim 1$, and thus $R_C = R_{sh}L_T/W$ and $R_T = R_{sh}(2L_T + L_{ch})/W$, where L_{ch} is the channel length. The linear fit of R_T *vs.* L_{ch} plot allows the extraction of $2R_C$, $2L_T$ and R_{sh} from the intersection with the R_T axis, L_{ch} axis and the slope, respectively. (iv) Four-probe measurements lead to $R_C = (V_{2p}/I_{sd} - (V_{4p}/I_{sd}) \times (L_{2p}/L_{4p})) \times W$, where W is the channel width and I_{sd}, V_{2p} (V_{4p}), and L_{2p} (L_{4p}) are the source-drain (probing contacts) current, voltage drops and length, respectively.[50] (v) Four-probe FET measurement avoids the potential drop in the sensing probes, and thus R_C can be extracted independently for each lead.[42] (vi) The Y-function method is more realistic since it allows the extraction of R_C from the FET linear region while considering phonon and surface scattering events as well as the voltage drop induced by the SB.[51]

2.3. Carrier injection at the metal/TMD contact

In the presence of a moderate SB, the main transport mechanism across the metal/TMD interface is thermionic emission, which can be described as

$$I = I_{2D}\exp(qV/\eta k_BT)[1 - \exp(-qV/k_BT)] \quad (1)$$

$$I_{2D} = WA^*_{2D}T^{3/2}\exp\left(-\frac{q\phi_B}{k_BT}\right), \quad (2)$$

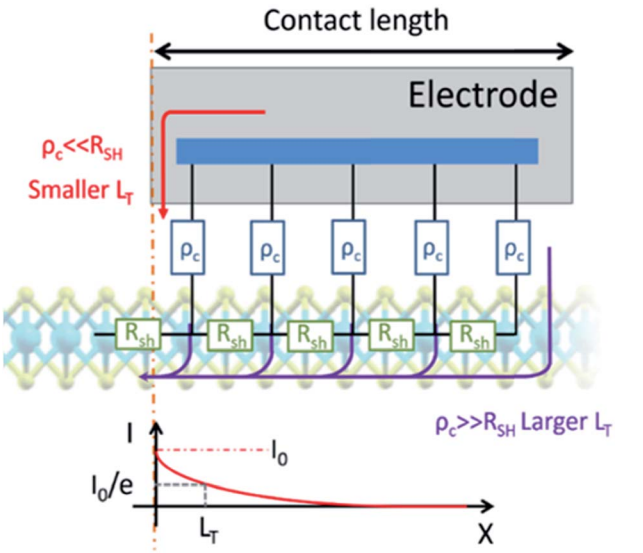

Fig. 3 Schematic view of current flow across metal/TMD junctions.

where I_{2D} is the saturation current, W is the junction length, q is the electron charge, ϕ_B is the SBH, η is the ideality factor, V is the voltage bias, and $A^*_{2D} = q\sqrt{8\pi k_B{}^3 m^*}/h^2$ is the 2D equivalent Richardson constant with m^* being the electron effective mass (Table 1).[24,49,52–54] It is also noteworthy that TMDs exhibit layer dependent effective mass, for instance the effective mass of MoS_2 varies from $0.41m_0$ to $0.57m_0$ from monolayer to few-layer.[55] At sufficient forward bias, the image charge-induced barrier lowering accounted for by the ideality factor can be extrapolated from $q/2.3\eta k_BT$ = slope of the linear fitting of the semilog I *vs.* V or $\log[I/(1 - \exp(-qV/k_BT))]$ *vs.* V plots.[54] Meanwhile, at sufficient reverse bias ($qV \gg k_BT$) $I \approx WA^*_{2D}T^{3/2}\exp(-q\phi_B/k_BT)$; therefore, SBH can be calculated from current–temperature measurements as $\phi_B = (k_B/q)(\Delta\ln(I/T^{3/2})/\Delta T^{-1})$ (Fig. 4a–c).[24,35] However, the veracity of the as-extracted SBH should be revised when $\phi_B < 3k_BT$ or $\phi_B < 0$ because such a SBH is not effective for carrier blocking.[31,56,57] Beyond thermionic emission, the applied bias configuration, doping level and temperature can enable direct tunneling (DT; field emission) through a wide-trapezoidal barrier at the quasi-Fermi level and/or thermally assisted Fowler–Nordheim tunneling (FNT; thermionic field emission) through a thin-triangular barrier above the Fermi level but below the top of the SB.[58] To discern whether DT or FNT dominates, the $\ln(I/V^2)$ *vs.* (I/V) plots should be explored as follows

$$I_{DT} = \frac{A_{eff}q^2V\sqrt{2m^*\phi_B}}{h^2d}\exp\left(\frac{-4\pi d\sqrt{2m^*\phi_B}}{h}\right) \quad (3)$$

$$\ln\left(\frac{I_{DT}}{V^2}\right) \propto \ln\left(\frac{1}{V}\right) - \frac{4\pi d\sqrt{2m^*\phi_B}}{h} \quad (4)$$

$$I_{FNT} = \frac{A_{eff}q^3m_0V^2}{8\pi h\phi_B d^2m^*}\exp\left(\frac{-8\pi d\sqrt{2m^*\phi_B{}^3}}{3hqV}\right) \quad (5)$$

$$\ln\left(\frac{I_{FNT}}{V^2}\right) \propto -\frac{1}{V}\left(\frac{8\pi d\sqrt{2m^*\phi_B{}^3}}{3hq}\right), \quad (6)$$

where d is the SB width.[59] Accordingly, the SBH can be evaluated by inspecting if the FNT (DT) shows a linear (exponential) trend

Table 1 Direct band gap (E_g [eV]), electron effective mass ($m^*_e[m_0]$), dielectric constant (ε [ε_0]), natural scaling length (λ [nm]) for 2 nm thick HfO_2 ($\varepsilon_{ox} = 25$), subthreshold slope (SS [mV dec^{-1}]), and drain-induced barrier lowering (DIBL [mV V^{-1}]) of monolayer TMDs.[94,95] Reproduced with permission from ref. 94 © 2013, *IEEE*; ref. 95 © 2014, *Applied Physics Letters*

TMD	E_g [eV]	$m^*_e[m_0]$	ε [ε_0]	λ [nm]	SS [mV dec^{-1}]	DIBL [mV V^{-1}]
MoS_2	1.8	0.56	4.8	0.41	~60	~10
$MoSe_2$	1.51	0.62	6.9	0.49	~65	~15
$MoTe_2$	1.10	0.64	8.0	0.54	~70	~20
WS_2	1.93	0.33	4.4	0.40	~60	~7
WSe_2	1.62	0.35	4.5	0.42	~63	~10

Open Access Article. Published on 24 September 2018. Downloaded on 10/19/2018 10:38:30 AM.
This article is licensed under a Creative Commons Attribution-NonCommercial 3.0 Unported Licence.

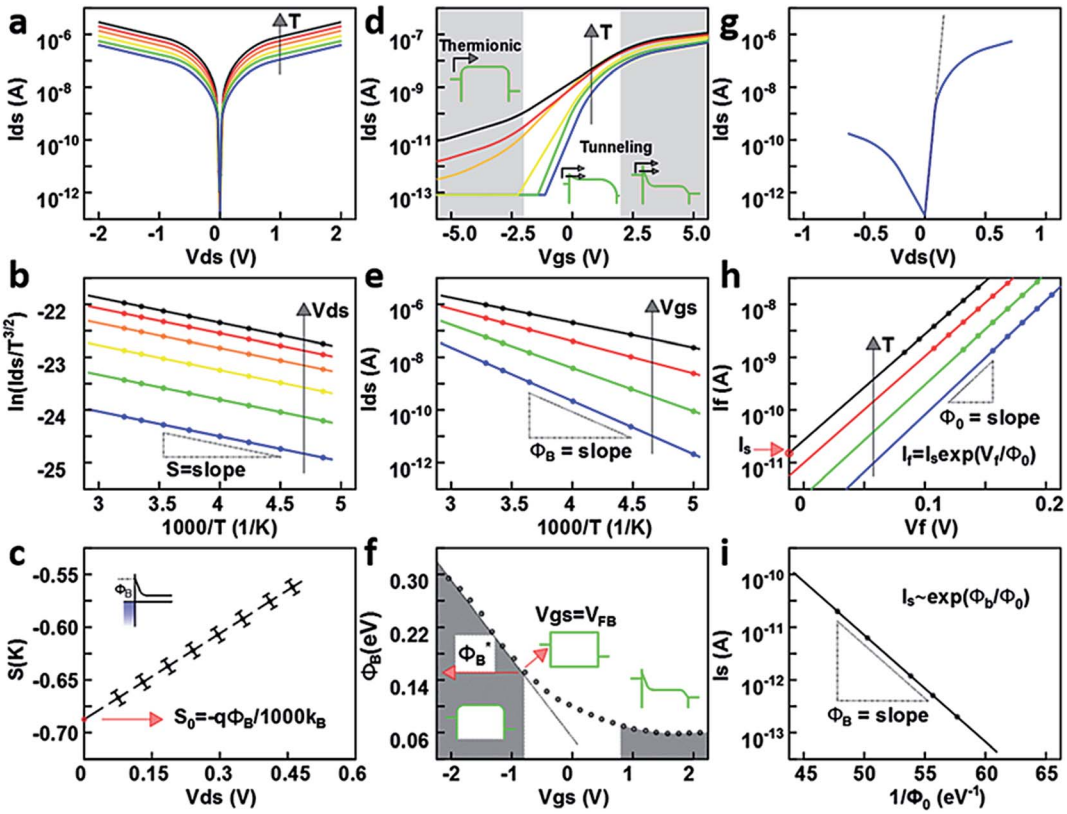

Fig. 4 SBH derivation of Co-contacted monolayer MoS_2 from (a) the I–V curve, (b) the Arrhenius plot, and (c) the slope (S) extracted from the Arrhenius plot.[35] SBH derivation of Ni-contacted 3 nm MoS_2 from (d) the transfer characteristics, (e) the Arrhenius plot, and (c) the extracted effective SBH as a function of the gate voltage.[23] SBH derivation of graphene-contacted WSe_2 from (g) the I–V curve, (h) the temperature dependent I_f–V_f plot, and (i) the slope extracted from the I_s *vs.* $1/\Phi_{00}$ plot.[64] Reproduced with permission from ref. 35 © 2013, American Chemical Society; ref. 23 © 2012, American Chemical Society; ref. 64 © 2014, American Chemical Society.

in the $\ln(I/V^2)$ *vs.* $(1/V)$ plot.[59,60] In fact, several groups have combined tunneling transport and FLP at the mid-gap to elucidate both the truly SBH, that is the flat band potential (V_{FB}), and the ambipolar behavior.[22–24,50,58,61–63] The method assumes thermally activated conduction through the channel as long as $V_{gs} < V_{FB}$, that is why the activation energy is linear with V_{gs}.[35,61] Thereby, the linear slope of semilog I_{ds} *vs.* $1/T$ plots elucidates the equivalent SB (ϕ_B^*) at different gate bias, and thus V_{FB} can be realized by finding at which V_{gs} the ϕ_B^* *vs.* V_{gs} deviates from linearity (Fig. 4d–f). Alternatively, the thermally assisted tunneling transport can be described as $I = I_s\exp(qV/\Phi_{00})$, where I_s is the saturation current at zero forward voltage and Φ_{00} is the characteristic energy, both being related as $I_s \propto \exp(\phi_B/\Phi_{00})$. Accordingly, I_s and Φ_{00} can be extracted from the linear fit of $\ln(I)$ *vs.* V at different temperatures, and ϕ_B can be extracted by the semi-logarithmic slope of I_s *vs.* $1/\Phi_{00}$ (Fig. 4g–i).[35,64]

2.4. Carrier mobility and carrier scattering effects

To investigate the intrinsic charge transport properties of TMDs, it is of paramount importance to properly assess the effective carrier mobility of high quality samples only limited by phonon scattering events. Precise mobility assessment can be done by Hall measurements, the Y-function method, and four-probe or two-probe based transconductance measurements but without R_C effects as follows, $\mu_{FE} = (LC_g/W)(\partial(1/(R_T - 2R_C))/\partial V_{gs})$, where L and W are the channel length and width, respectively.[51,65–67] Nevertheless, the presence of Coulomb impurities at the TMD/dielectric interface and defects in low quality samples as well as the substrate roughness affect notoriously the mobility.[30] According to Matthiessen's rule, the overall scattered-limited mobility becomes $\mu(\mathrm{n,T})^{-1} = \mu_{\mathrm{Coulomb}}(\mathrm{n,T})^{-1} + \mu_{\mathrm{ph}}(\mathrm{T})^{-1} + \mu_{\mathrm{sr}}^{-1}$ where μ_{Coulomb}, μ_{ph} and μ_{sr} are the Coulomb scattering, phonon scattering, and surface roughness phonon scattering, respectively.[20,25,68] At low temperatures, the mobility is mostly limited by Coulomb scattering arising from ionized impurity charges fixed at the bottom substrate.[69] Moreover, the Coulomb scattering is highly intensified in monolayer TMDs due to the short-interaction distance between impurities and carriers. Indeed, an increasing number of layers lead to a higher dielectric constant and charge redistribution far from the interface; as a result, the outer layer experiences reduced Coulomb scattering leading to mobility peaking at ~10–15 layers.[20,25,29,68,70–74] In this regard, experimental results have evidenced Hall mobilities up to 1000 (34 000) $cm^2\ V^{-1}\ s^{-1}$ for 1L (6L) MoS_2 at 5 K.[25,26,75] At higher temperatures, the electron–phonon interaction becomes dominant, leading to phonon-limited carrier mobility.[76,77] The phonon scattering temperature dependence follows the power

 This journal is © The Royal Society of Chemistry 2018

Open Access Article. Published on 24 September 2018. Downloaded on 10/19/2018 10:38:30 AM.
This article is licensed under a Creative Commons Attribution-NonCommercial 3.0 Unported Licence.

law $\mu_{ph} \propto T^{-\gamma}$ with γ ranging from 0.55 to 1.7 for MoS_2 (ref. 27, 75 and 78) and 0.73 to 1.75 for WS_2.[79] The upper bond mobility limit is determined by the large effective mass and out-of-plane polar phonons (*i.e.* 410 $cm^2\ V^{-1}\ s^{-1}$ for 1L MoS_2).[30,80] Nevertheless, the highest mobilities reported to date at room temperature are 190 (700) $cm^2\ V^{-1}\ s^{-1}$ for monolayer (10 nm) MoS_2,[23,81] and ~250 $cm^2\ V^{-1}\ s^{-1}$ for monolayer WSe_2.[82] On the other hand, atomically flat TMDs exhibit negligible surface scattering, in contrast to the severe surface scattering exhibited by 5 nm rough ultrathin Si.[30]

2.5. Carrier transport and the scattering limited mobility-edge concept

To this extent, the mobility-edge concept, a boundary in the band tail that discriminates between extended and localized states, establishes a useful tool to assess the transport mechanism.[28] Extended states enable metallic band-like transport characterized by decreasing mobility with increasing temperature, whereas deep (local) localized states elucidate insulating variable range hopping (thermally activated) transport characterized by increasing mobility with increasing temperature (Fig. 5a). As the gate bias continuously modulates the Fermi energy from localized states to extended states, a metal-to-insulator transition (MIT) can be observed at the threshold carrier concentration.[27,83] Below a certain carrier-density limit, the Fermi level lies on deep localized states caused by short-range disorder, leading to electrons flowing by phonon limited thermally activated nearest-neighbor hopping (NNH) conduction at high temperature,[84] where k_BT_1 is the energy spacing between the nearest neighbors, or by weak temperature dependent variable-range hopping (VRH) conduction at low temperature, where T_0 is the correlation energy, and d is the material dimensionality ($d = 2$ for 2D-TMDs).[70–72,85–87] However, as the Fermi level moves toward the conduction band localized states are filled and when the Fermi level enters the band-tail carriers become mobile, enabling band-like conduction.[71] Alternatively, thermally activated carriers from shallow localized states to the conduction band enable band-like conduction, where E_a is the activation energy.[27]

2.6. Short channel effects and ballistic transport

Typically, the carrier concentration of bulk semiconductors cannot be fully tuned by gate bias because the electric potential is not uniform across the thick bulk semiconductor. In contrast, the dangling-bond free nature and ultrathin structure of 2D-TMDs lead to highly confined carrier distribution close to the gate dielectric and highly uniform potential distribution along the channel, thus allowing homogeneous gating (Fig. 5b).[29] Consequently, the drain–source electric field lines fall mostly on the surrounding environment, and thus the semiconductor depletion depth can be replaced by the TMD thickness (t_{body}) and the semiconductor dielectric constant can be regarded as the environment (Fig. 5b).[88–90] The electrostatic integrity can be evaluated by the drain-induced barrier lowering, where low drain-induced barrier lowering (DIBL) yields robustness against short channel effects (SCE).[18,28,43,88] Indeed, to suppress SCEs

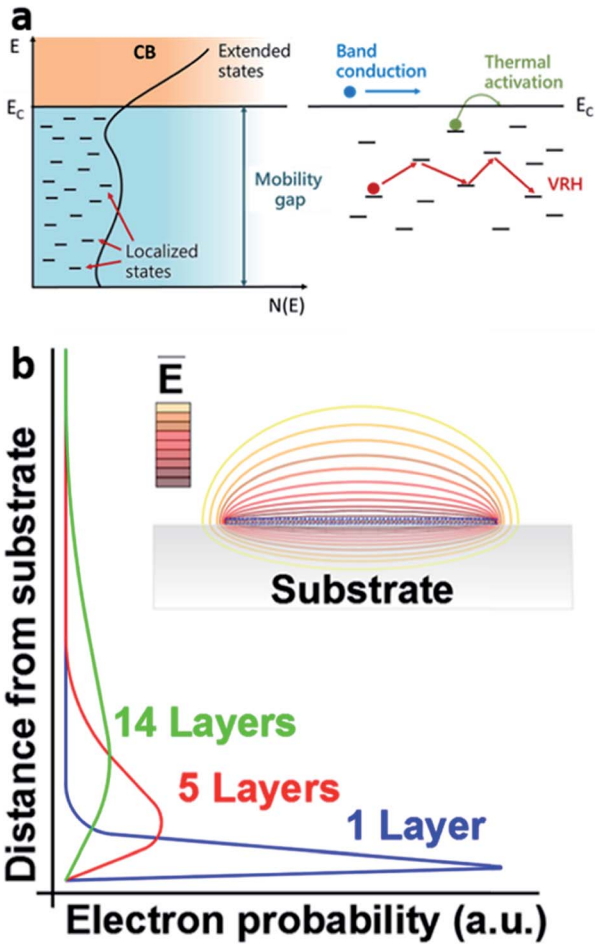

Fig. 5 (a) Mobility edge concept for carrier transport *via* hopping (thermal activation) at deep (shallow) localized states or band transport at extended edge states. (b) Carrier distribution in 1, 5, and 14 layer channels.[29] Inset: illustration of equipotential electric field lines along the channel.[90] Reproduced with permission from ref. 29 and 90 © 2013, American Chemical Society.

and hence preserve the long channel behavior, the channel length should be at least 4–5 times longer than the electrostatic natural scaling screening length, a figure of merit to distinguish between short and long channel behaviors, where t_{ox} and ε_{ox} are the thickness and dielectric constant of the gate oxide.[28,58,73,88,91] Therefore, the rather low screening length enables gate tuning of the carrier concentration $n = C_g(V_g - V_{th} - V_{ds})/q$, where the gate capacitance C_g should include the oxide capacitance (C_{ox}), the TMD quantum capacitance (C_q), and the interface trap density capacitance, where D_{it} is the trap density.[18,28,32,89,92] Nonetheless, in a double-gated geometry C_g should include both top and bottom gate capacitances.[25,31,42,65,66,73] Furthermore, as the channel length is scaled down to the electron mean free path, electronic devices are pushed from the diffusion limit to the scattering-free ballistic limit, at which the quantum conductance can potentially reach $2e^2/h$ and the quantum contact resistance can reach 30 Ω μm at a n_{2D} of 10^{13} cm^{-2}.[22,93]

To gain further insight on the SCE and ballistic transport characteristics of TMDs, Table 1 shows the λ, SS and DIBL calculated from ballistic transport simulations of scattering-free

Open Access Article. Published on 24 September 2018. Downloaded on 10/19/2018 10:38:30 AM.
This article is licensed under a Creative Commons Attribution-NonCommercial 3.0 Unported Licence.

15 nm short channels of monolayer TMDs with 2 nm thick HfO_2 ($\varepsilon_{ox} = 25$).[94,95] The extremely low $\lambda < 0.5$ nm causes a highly intensified electric field at TMD/contact junctions, enabling the possibility to devise tunnel transistors with a high on-current of $\sim$500 μA μm^{-1} by engineering the TMD bandgap and effective mass.[95] In addition, negative differential resistance (NDR) can be found along ballistic transport due to the narrow energy dispersion of the TMD bands and the reduction of available states in the drain.[94,96] Meanwhile, the SS of $\sim$60 mV dec^{-1} and DIBL of $\sim$10 mV V^{-1} suggest that at the monolayer limit the dielectric environment still dominates the vertical electric field regardless of the TMD dielectric constant.[43,94,97] Among the TMDs, the lower electron effective mass and dielectric constant of MoS_2, WS_2 and WSe_2 than those of $MoSe_2$ and $MoTe_2$ lead to the lowest SS and DIBL due to the diminished influence of the drain-triggered lateral electric field.[94] Accordingly, the large bandgap and relatively high effective mass of monolayer MoS_2 offer a significant on–off ratio, 52% lower DIBL and 13% lower SS than 3 nm Si at 10 nm channel length, and can lead to the DIBL of 100 mV V^{-1} of ITRS at 8 nm compared to 10 nm Si;[97] nevertheless, the lower mobility than most III–V materials makes MoS_2 more suited for low standby and operating power than high performance FETs.[43] Furthermore, highly scaled p-WSe_2 can meet the on-current ITRS requirements for high-performance p-FETs.[98] However, monolayer TMDs still offer relatively lower performance than hydrogenated silicene (*i.e.* silicane).[98] On the other hand, the shortest channels experimentally fabricated so far are 10 nm-MoS_2/graphene and 7.5 nm 2H/1T MoS_2 trenches, which have revealed a SS of 90–120 mV dec^{-1}, an off-current of 10 pA μm^{-1}, and an on–off ratio of 10^6–10^7.[91,99] Alternatively, ultrashort effective channel lengths developed by top-gated FETs with 10 nm width air-oxidized Al stripes lead to a SS of 80 mV dec^{-1} with a high on-current of 400 μA μm^{-1},[100] whereas 1 nm carbon nanotube metal gates have led to a SS of 65 mV dec^{-1} and an on–off ratio of 10^6.[101] Besides MoS_2, dual gated BN-encapsulated and graphene-contacted WSe_2 with 100 nm local gates has enabled Klein tunneling of Dirac fermions at 20 mK, resembling Fabry–Pérot oscillations and thus suggesting ballistic transport at the local gate.[102]

3. Carrier injection and carrier transport engineering strategies

We next discuss several engineering strategies to overcome the aforementioned carrier injection and carrier transport limitations toward improving the electronic properties of TMDs. The strategies can be divided roughly into three engineering categories: contact, dielectric and material (Fig. 6a). As low R_C is compulsory for efficient carrier transport, we first focus on the contact geometry and how metals and interlayers can further improve R_C and different transport aspects. Second, we focus on how surface defects and adsorbates affect the intrinsic electronic properties of the conducting channel, and how the surrounding dielectric passivates scattering centers and tune the electronic transport. Third, we present distinct doping techniques, plasma treatments and phase transformation approaches to tailor the electronic properties of TMDs. To grasp the great throughput of these strategies, Fig. 6b highlights the most remarkable achievements obtained by specific strategies that we detail in the next subsections.

3.1. Contact geometry engineering

The metal/TMD contact geometry either face-contact or edge-contact also plays a key role in the contact properties.[22,37] In the face-contact mode, the direct metal deposition onto TMD fractures covalent bonds and originates defects, enhancing R_C due to FLP and high SB. However, transferred metals on 2D-TMDs circumvent the FLP, leading to well-controlled SBs by the Schottky–Mott rule.[40] Alternatively, conductive 2D-metals with a wide range of work functions (Fig. 1) offer the possibility to eliminate metal-induced gap states and unbroken covalent bonds by vertically stacking them on 2D-TMDs *via* vdW forces, thus reducing FLP and enabling tunable SB for both electrons and holes (Fig. 7a–c). For example, thermally stable degenerate $Nb_{0.005}W_{0.995}Se_2/WSe_2$ contacts offer an extremely low R_C of 300 Ω μm, a world record on–off ratio of 10^9, an on-current of 320 μA μm^{-1} and mobilities of 200 and 2000 cm^2 V^{-1} s^{-2} at 300 K and 5 K respectively.[103] Similarly, 2D metallic $NbSe_2/WSe_2$ elucidates ohmic contacts from direct tunneling through lowered SB (Fig. 1).[104] More interestingly, graphene as a face-contact material can reduce R_C dynamically by pumping charge *via* band alignment modulation.[105] On the other hand, edge-contact devised by atomically sharp interfaces strongly reduces the FLP and enables control over the SB.[106] To realize edge-contact, several techniques have been formulated as follows (Fig. 7d–f). (i) BN-sandwiched TMDs provide 1D atomic edge ohmic contacts with superior mobility and stability.[26,50] (ii) Aromatic molecule-assisted in-plane atomic stitching enables large-scale graphene/MoS_2 with a R_C of 300 Ω μm.[107] (iii) Epitaxial growth of lateral graphene/MoS_2, graphene/WSe_2 and graphene/WS_2 heterostructures results in R_C as low as 11 kΩ μm, 50 kΩ μm and 30 kΩ μm, respectively.[108–110] (iv) Degenerate edge contacts by alloying (*i.e.* $W_xNb_{1-x}Se_2/WSe_2$) or chemical doping (*i.e.* NO_2-doped p$^+$ WSe_2, K-doped n^+ WSe_2, and P-doped p$^+$-MoS_2) lead to low interface-trap density ohmic contacts.[82,111–113] (v) 2D-TMD lateral heterojunctions.[114,115] (vi) Phase transformation yields low SB due to the close band alignment between the metallic-phase work function and the semiconducting-phase conduction band, enabling R_C as low as 200 Ω μm.[116] (vii) Semiconducting to metallic/semimetallic transitions from monolayer to multilayer in noble-TMDs such as $PtSe_2$ and PdS_2 owing to the strong interlayer bonding allow the fabrication of single-material nanoelectronic devices with low leakage current and extremely low contact resistance down to 70 Ω μm.[117–119]

3.2. Metal contact engineering

The dangling bond-free nature and ultra-thin structure of 2D TMDs do not lead to the formation of any chemical bond with metals; however, the native defects of TMDs induce Fermi level shifts of 1 eV over nanometer scale areas regardless of the metal contact work function (Fig. 1), providing low SBs that in turn

 This journal is © The Royal Society of Chemistry 2018

Open Access Article. Published on 24 September 2018. Downloaded on 10/19/2018 10:38:30 AM.
This article is licensed under a Creative Commons Attribution-NonCommercial 3.0 Unported Licence.

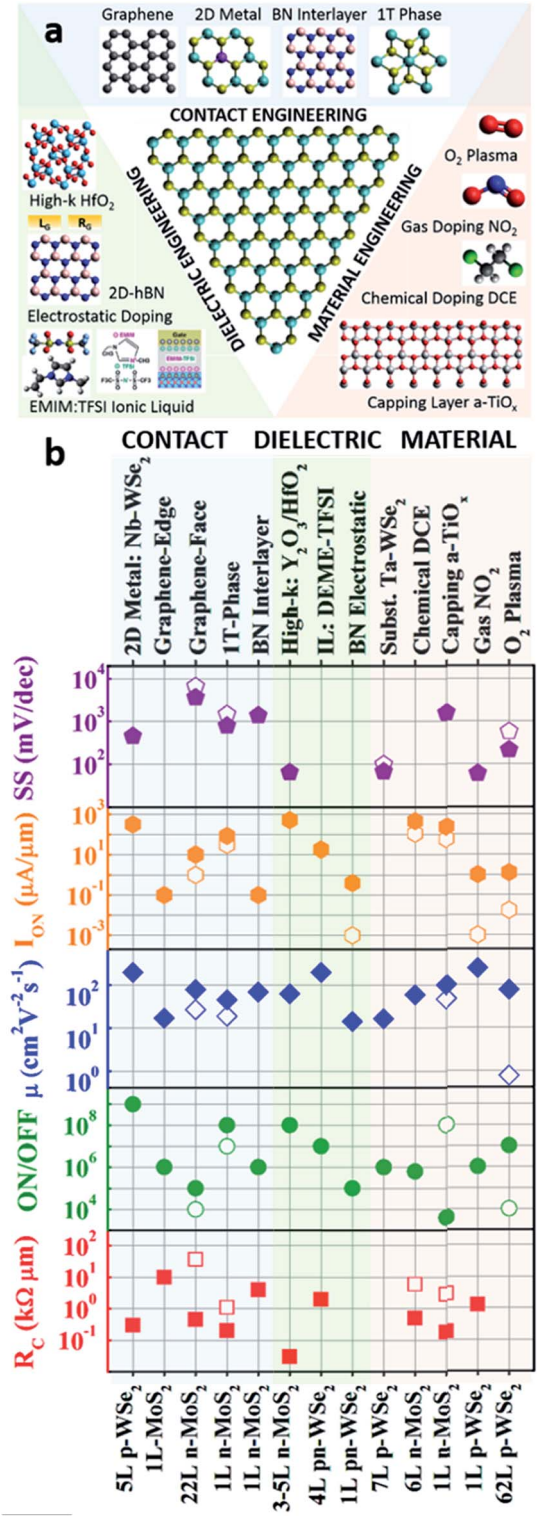

Fig. 6 (a) Contact, dielectric and material engineering strategies to tune the carrier injection and carrier transport of 2D-TMDs. (b) The most remarkable improved contact resistance and FET characteristics of TMDs to date by engineering strategies; empty and filled symbols indicate before and after applying the strategy, respectively. Contact engineering: Nb–WSe_2 2D metal contact,[103] graphene-edge and -face contacts,[108,124] 1T-phase contacts,[116] and BN interlayer inclusion.[50] Dielectric engineering: stacked high-*k* Y_2O_3/HfO_2 dielectrics,[32] DEME-TFSI ionic liquid,[64] and electrostatic doping based on dual gate atomically thin BN (empty symbol: hole, filled symbol: electron).[212] Material engineering: Ta-doped p-WSe_2 *via* substitutional doping,[170] 1,2-dichloroethane (DCE) based chemical doping,[185] surface charge-transfer *via* amorphous-titanium suboxide (a-TiO_x) capping layer,[184] molecular NO_2 gas doping,[82] and oxygen plasma treatment.[191]

reduce R_C and boost the on-current *via* band-tunneling while preserving the SS value.[120,121] Moreover, metal-induced doping *via* narrow bandgap or metallic surface state formation can also shift the Fermi level, and thus alleviate the interfacial barrier.[41] For example, Al (Ag) onto monolayer WSe_2 greatly (slightly) shifts the Fermi level toward the conduction band, indicating weak (strong) electron doping characteristics due to the low (high) density of states of Al (Ag) near the WSe_2 Fermi level.[122] Therefore, the prospective choice of metals with the optimal work function can engineer ohmic contacts with negligible R_C. For instance, In and Ag metals having a work function close to the electron affinity of WSe_2 form low resistant n-type ohmic contacts with ambipolar WSe_2, leading to an on-current of 210 $\mu A\ \mu m^{-1}$.[122] Similarly, Sc or Ti (Pt) metals with a low (high) work function of 3.5 or 4.3 eV (5.9 eV) contacting multilayer MoS_2 can form ohmic (Schottky) contacts; as a consequence, the Sc-ohmic contact affords highly effective mobilities of 700 $cm^2\ V^{-1}\ s^{-1}$ (Fig. 7g).[23] More interestingly, Pd-contacted few-layer MoS_2 results in p-type doping, leading to the photovoltaic effect by contacting the other side with Au.[123] Nevertheless, transferred Ag (Pt) electrodes on MoS_2 that avoid the FLP effect lead to 20 (67) meV electron (hole) SBs, enabling 260 (175) $cm^2\ V^{-1}\ s^{-1}$ electron (hole) mobilities and 0.66 (0.21) mA μm^{-1} on-current.[40] However, the Fermi level of bulk metals is fixed due to the vast sea of electron concentrations, and thus it is not tunable by electrostatic gating. Conversely, graphene offers not only a gate-tunable Fermi level but also an interfacial layer to avoid metal-induced damage, leading to an extremely low R_C of 200 Ω μm (Fig. 7i).[64,124] Furthermore, vacuum annealing engineering is a proven tool to improve R_C.[125] For example, varying from ultra-high vacuum (10^{-9} Torr) to high vacuum (10^{-6} Torr) during Au, Cr, Ir, Sc metal deposition strongly influences R_C due to the chemical nature of the interface (*i.e.*, covalent bonds, vdW gaps, or permalloys).[126,127]

3.3. Metal/TMD interface engineering

Interface engineering is a promising strategy to modulate the metal/TMD SB. As striking consequences, the R_C can be highly reduced *via* FLP annihilation, and the channel can be populated with both electrons and holes toward ambipolar conduction. In fact, DFT calculations predict that 0.6 nm vdW-gaps can precisely tune the metal work function-dependent SB.[38] Furthermore, electrons tunneling through dangling bond-free ultrathin boron nitride (BN) interlayers can annihilate the FLP and enable SB tunability while preserving the intrinsic MoS_2 band structure, thus leading to reversible gate tunable ambipolar p–n junctions (Fig. 7h).[39,50,128] Alternatively, metal oxides provide a fruitful path to unpin the Fermi level. For example, high work function metal Pd/MoO_x/MoS_2 contacts or the Co catalytic oxidation of multilayer MoS_2 into MoO_x nanoparticles can enable ambipolar transport owing to efficient hole injection

Open Access Article. Published on 24 September 2018. Downloaded on 10/19/2018 10:38:30 AM.
This article is licensed under a Creative Commons Attribution-NonCommercial 3.0 Unported Licence.

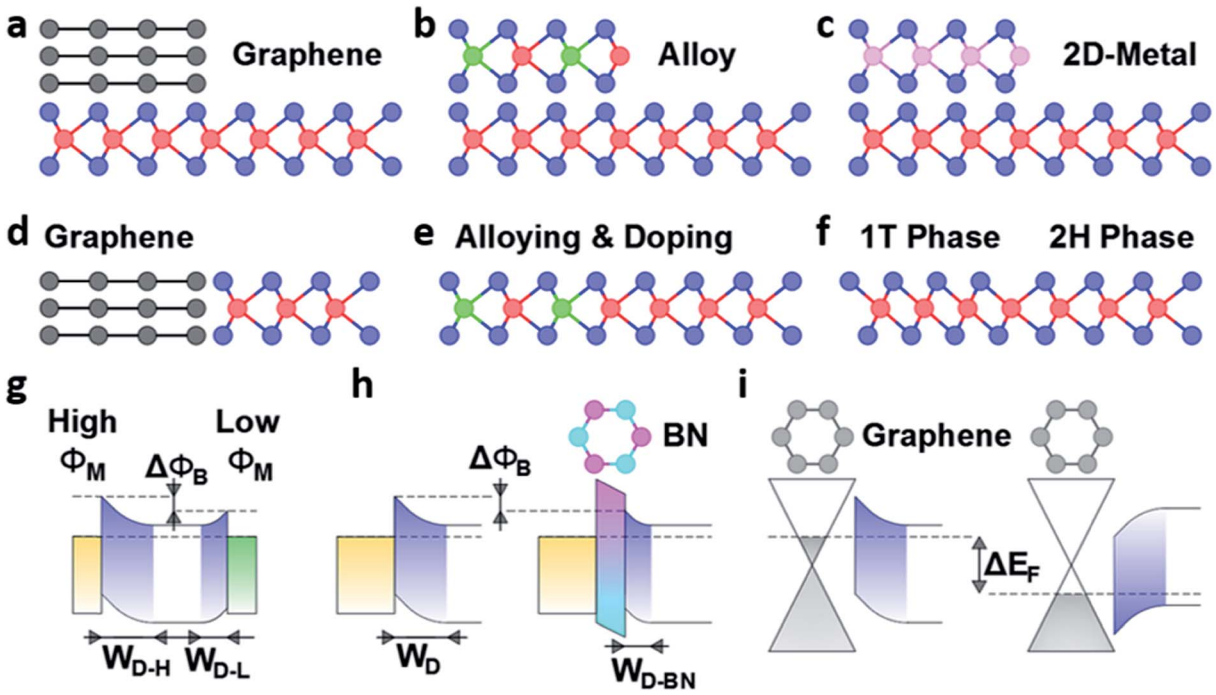

Fig. 7 Contact geometry strategies to improve 2D-TMD contacts. Face contacts: (a) graphene, (b) alloy, and (c) 2D metal. Edge contacts: (d) graphene, (e) alloying and doping, and (f) 2H to 1T phase transformation. Illustration of 2D-TMD/metal contact strategies to tune the SB and depletion width. (g) High *versus* low metal work function, (h) ultra-thin interfacial layers such as boron nitride (BN), and (i) gate-tunable graphene Fermi level.

into MoS_2; consequently asymmetric Ni/MoS_2/MoO_x/Pd diodes show a rectification ratio of 10^5 and an ideality factor of 1.4.[129,130] Furthermore, the insertion of TiO_2 or MgO thin films between a ferromagnetic Co electrode and MoS_2 significantly lowers the SB toward efficient spin tunnel contacts, leading to a 100-fold on–off ratio and 7-fold mobility enhancements.[35,63] Similarly, 2 nm ultrathin TiO_2 or Al_2O_3 interlayers can unpin Ti, Ni, Au and Pd metals from MoS_2, and thus reduce the SB by shifting the Fermi level toward the conduction band; consequently, L_T substantial reduces to 280 nm, inducing 5–24 fold R_C reduction as well as 10-fold mobility and 5-fold on-current enhancements.[131,132] A more subtle technique to reversibly modulate the contact resistance by 4 orders of magnitude is by exerting vertical compression *via* the tip force of a conductive atomic force microscope owing to the enhanced quantum tunneling.[133] For instance, depending on the compressive load applied on a MoS_2/graphene system a small band gap up to 12 meV can be induced within the band structure, thus significantly reducing the SBH and increasing the electron density which improve the current injection.[134]

3.4. TMD surface engineering

The high surface-to-volume ratio and ultra-thin structure of TMDs make their intrinsic physical and chemical properties highly sensitive to perturbations in the lattice structure, similar to low-dimensionality oxide nanostructures.[135–137] Particularly, the TMD work function governs the band bending at the metal/TMD interface and hence the charge transport. The MoS_2 work function highly varies with distinct atmospheric conditions (4.36 eV for ambient, 4.04 eV for UHV and 4.47 eV for O_2), indicating that adsorbents are strong enough to modulate the electronic energy levels in MoS_2; consequently, the charge transport under ambient, low vacuum, and high vacuum conditions is dominated by thermionic, thermionic-tunneling, and tunneling transport, respectively.[138] In fact, physisorption and chemisorption of both water and oxygen have been reported to deplete electrons in n-type TMDs, thus inducing p-doping and weakening the electrostatic screening; conversely, holes are accumulated in p-type TMDs, leading to stronger p-type behavior.[139,140] Consequently, the on-current of MoS_2 degrades by two orders of magnitude, suggesting that the adsorption of gas molecules at surface defects is an efficient molecular gating strategy with superior control over the charge density than electrostatic gating. Nonetheless, the device performance can be recovered by desorbing adsorbates *via* vacuum annealing.[79,140] However, there is some discrepancy regarding the oxygen adsorption on MoS_2. For instance, Qi *et al.* pointed out that after diminishing the effect of physically adsorbed oxygen molecules almost to zero by using a UHV system with a well-controlled oxygen partial pressure, solely the effect of oxygen chemisorption on surface defects of few layer MoS_2 results in n-doping without mobility degradation owing to the dissociative adsorption of oxygen, which lowers the conduction band edge locally.[141] Furthermore, Komsa *et al.* deliberately created sulfur vacancies on monolayer MoS_2 by electron-beam irradiation and studied whether they could be filled by oxygen and other species to induce doping; as

 This journal is © The Royal Society of Chemistry 2018

Open Access Article. Published on 24 September 2018. Downloaded on 10/19/2018 10:38:30 AM.
This article is licensed under a Creative Commons Attribution-NonCommercial 3.0 Unported Licence.

a consequence they showed that substitutional oxygen at sulfur vacancies does not produce any localized state in the gap region, whereas N, P, As and Sb behave as acceptors and F, Cl, Br, and I behave as donors.[142] Alternatively, Mahdi *et al.* showed that the combination of angle-dependent and ion-type beam-irradiation and post-exposure to precursors gases could be used to induce doping as well, and thus tune the electronic properties towards for example negative differential resistance.[143]

3.5. Solid state dielectric engineering

Typically, gate dielectrics are responsible for slow and fast charged traps that lead to severe reliability issues such as hysteresis and temperature instabilities, respectively. In this regard, pristine-BN substrates mitigate hysteresis *via* slow trap suppression but deteriorate the temperature dependence due to thermally activated traps.[144] Moreover, localized states owing to defective gate dielectrics have been regarded as the origin of the ambipolar conductivity of MoS_2 (Fig. 8a).[145] Interestingly, multilayer MoS_2 on PMMA (SiO_2) exhibits ambipolar (unipolar) transport with high (low) mobilities, suggesting that long (short) range disorder dominates PMMA (SiO_2) dielectrics.[146] On the other hand, high-*k* gate dielectrics such as HfO_2, ZrO_2, and Al_2O_3 allow not only broad carrier density modulation ($\sim 10^{10}$–10^{13} cm^{-2}) to enable band-transport, but also high carrier mobility enhancement due to the suppression of Coulomb scattering and optical phonon modes (Fig. 8b); for instance 10 nm Al_2O_3 (30 nm HfO_2) top gated 23L (1L) n-MoS_2 achieves a remarkable mobility of 517 (217) $cm^2\ V^{-1}\ s^{-1}$ with an on–off ratio of 10^8.[10,25,29,69,147,148] However, the high dissociative activation energy between HfO_2 and MoS_2 leads to substantial leakage current; as a solution, buffer layers such as Mg, Al_2O_3, Y_2O_3 improve the conformability between HfO_2 and MoS_2. Accordingly, Y_2O_3/HfO_2 stacks exhibit high-quality interfaces with a low D_{it} of $\sim 2 \times 10^{12}$ $cm^{-2}\ eV^{-1}$, thus yielding a SS of 65 mV dec^{-1} and a saturation on-current of 526 $\mu A\ \mu m^{-1}$.[32] An alternative to high-*k* dielectrics is atomically flat BN with a relative permittivity of 3.5 (close to 3.9 of SiO_2) enabling room temperature mobilities of 140, 214, 151 $cm^2\ V^{-1}\ s^{-1}$ with on–off ratios of 10^6 to 10^7 in 3L p-WSe_2, 1L n-WS_2, and 1L n-MoS_2, respectively.[149–151]

3.6. Ionic liquid and polymer electrolyte engineering

Ionic liquids (ILs) and polymer electrolytes (PE) are cationic–anionic binary organic salts and polymers that under positive (negative) gate bias can accumulate negative (positive) and positive (negative) charge on the gate or TMD channel, respectively (Fig. 8c).[152–154] Consequently, ultrathin (~1 nm) spatial charge doublets form at the interface, leading to electric double layers (EDLs) that mimic nanogap capacitors with extremely high capacitance ($\sim 100\ \mu F\ cm^{-2}$).[152,155] The strong gate-channel coupling in combination with solid state back gates allows fine Fermi level tuning across the whole bandgap, and thus makes it possible to access quasi-continuously a large range of carrier densities up to 10^{14} cm^{-2}.[152,153,155,156] Such fine carrier density tuning capability enables the investigation of novel intriguing properties and phenomena, as we next enumerate. (i) Charge transfer between the electrolyte and TMD takes place until the

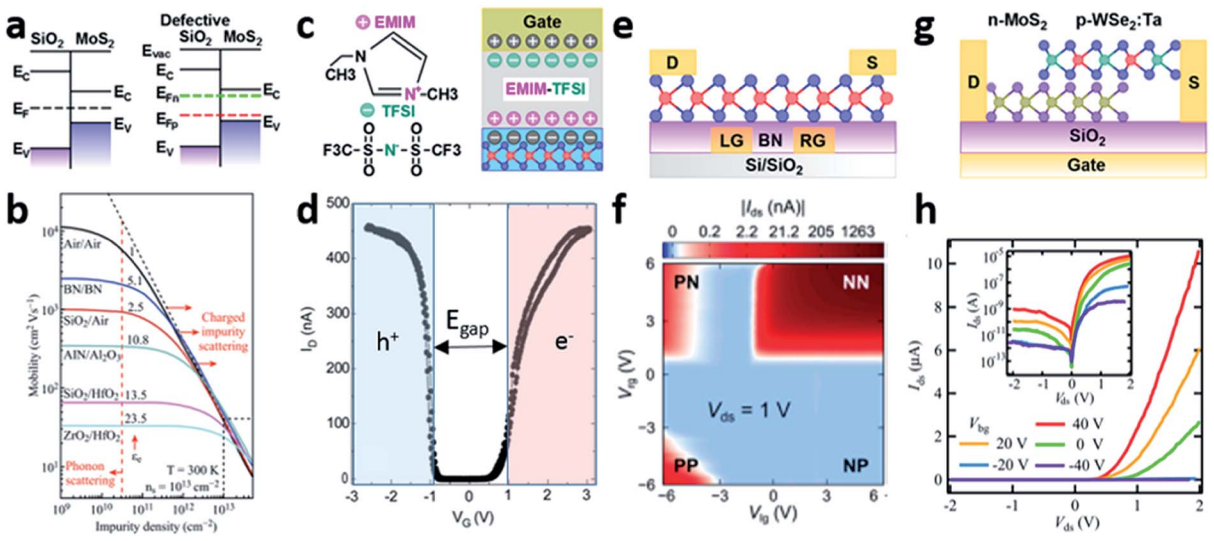

Fig. 8 Dielectric engineering: (a) schematic of the MoS_2 band diagram on defective SiO_2 with either donor (green line) or acceptor (red line) states, showing the n- or p-type conduction modulation,[145] and (b) the net electron mobility at room temperature of monolayer MoS_2 surrounded by different dielectrics and considering different scattering mechanisms.[69] Ionic gating: (c) schematic of the EMIM-TFSI ionic liquid and ionic gate effect, and (d) ionic gate transfer characteristics of WSe_2 indicating the bandgap estimation from the ambipolar transport.[157] Electrostatic doping: (e) device schematic of the left and right gate (LG, and RG) configuration, and (f) color maps of the left and right gate transfer characteristics of WSe_2 highlighting the PP, NN, NP, and PN behaviors.[164] Substitutional doping: (g) schematic of a p-WSe_2:Ta/n-MoS_2 heterostructure, and (h) the gate tunable rectifying characteristics.[170] Reproduced with permission from ref. 145 © 2013, American Physical Society; ref. 69 © 2014, American Physical Society; ref. 157 © 2012, American Chemical Society; ref. 164 © 2014, American Chemical Society; ref. 170 © 2017, American Institute of Physics.

Open Access Article. Published on 24 September 2018. Downloaded on 10/19/2018 10:38:30 AM.
This article is licensed under a Creative Commons Attribution-NonCommercial 3.0 Unported Licence.

electrolyte redox potential aligns with the TMD Fermi level; consequently, the band bending induced by the space charge reduces the contact barrier and facilitates tunneling carrier injection, boosting the mobility and reducing the subthreshold slope down to 62 mV dec^{-1}.[152,155,157,158] (ii) Ambipolar transport has enabled the possibility to find holes with higher mobility than electrons in MoS_2 as well as to quantitatively determine the band gap based on the electron–hole threshold voltage difference (Fig. 8d).[157,159,160] (iii) Ambipolar transistors operating beyond the electron saturation regime, where electrons and holes are injected from opposite contacts, have been used to devise stable pn junctions at temperatures below the glass transition temperature that emit either unpolarized or Zeeman-type circularly polarized light.[159–162] (iv) Gate-induced MIT transitions followed by superconductivity with enhanced transition temperature.[155,156]

3.7. Doping engineering

Doping is the most universal technique to control the carrier type and carrier concentration in the semiconductor industry and thus enable versatile electronic devices. Nevertheless, the conventional techniques used to dope bulk semiconductors (*i.e.* Si or GaAs) such as dopant diffusion or ion-implantation are not suitable for novel 2D materials such as layered TMDs due to the induced damage. Consequently, alternative doping strategies are required. Therefore, we next review the most successful engineering strategies to precisely control the doping level.

3.7.1. Electrostatic doping. Electrostatic doping, characterized by external perpendicular electric field-induced charge transfer, can tune the electrical transport without introducing disorder and causing defects. Moreover, the charge transfer is reversible and offers long-term stability. In this regard, the 2D nature and weak dielectric screening characteristics of TMDs enable improved electrostatic control than those of 3D materials to finely tune the Fermi level across the electronic bandgap.[58] Therefore, symmetric dual local gate structures shed light to tailor the depletion width at the source and drain contacts independently, and thus reconfigure TMDs from metallic isotype (p–p, n–n) to rectifying anisotype (p–n and n–p) behaviors toward multifunctional devices (Fig. 8e and f).[163–167] Additionally, owing to the thickness dependence of TMDs, the gate bias effect on L_T must be carefully addressed to avoid detrimental impact on R_C prospects.[46,47,132]

3.7.2. Substitutional doping. Substitutional doping, characterized by replacement of host atoms by dopant atoms, is one of the most common strategies. In this regard, controlled soft phosphor plasma can induce a broad range of p-type doping in MoS_2 with minimum surface damage, and thus form high quality pn junctions with unexposed n-MoS_2.[113] Alternatively, adjusting the molar ratio of source materials or intercalating metal/dopant/metal stacks during chemical vapor growth could yield specific doping ratios of the desired crystals.[168,169] On this point, Nb with a similar ionic radius and oxidation state to Mo, only one valence electron less than Mo, is a perfect acceptor candidate for either MoS_2 or $MoSe_2$; therefore, Nb–MoS_2 has enabled different degrees of p-type doping from degenerate for ohmic contacts to non-degenerate for pn junctions and ambipolar FETs.[168,169] Similarly, Ta matches the ionic radius and oxidation state of W, leading to excellent p-type behavior; thereby, p-$Ta_{0.01}W_{0.99}Se_2$/n-MoS_2 yields an impressive rectification ratio of 10^5 with an ideality factor of 1 (Fig. 8g and h).[170]

3.7.3. Chemical doping. Molecular absorption-induced chemical doping is a high-throughput tool that can modulate the carrier concentration and shift the Fermi level of the host material *via* surface charge-transfer while preserving the electronic properties without inducing defects. Considering that the electronegativity (χ) measures the electron attraction tendency of a medium, the surface charge-transfer process between two media can be understood by the electronegativity differences, which determine the net charge flow direction and thus which medium becomes the electron donor or acceptor. Therefore, the higher electronegativity medium withdraws electrons from the other, and the larger the electronegativity difference, the larger the amount of transferred electrons. The dopant molecule electronegativity is defined as $\chi_{mol} = 1/2(IP + EA)$, where IP is the first ionization potential (the energy to withdraw an electron and form a cation, which is equal to the negative of the highest occupied molecular orbital (HOMO)), and EA is the electron affinity (the energy needed to withdraw an electron from an anion, which is equal to the negative of the lowest unoccupied molecular orbital (LUMO)).[171] On the other hand, the TMD electronegativity $\chi_{TMD} = E_{VBM} + E_e - 0.5E_g$, where E_{VBM} is the valence band maximum (VBM) potential against the normal hydrogen electrode (NHE), E_e (~4.5 eV) is the free electron energy on the hydrogen scale (*i.e.* the standard electrode potential on the NHE scale), and E_g is the bandgap. In this regard, Fig. 1 shows the band alignment of monolayer TMDs and the water reduction (H^+/H_2) and oxidation (H_2O/O_2) potential with respect to the vacuum level.[172] It is noteworthy that the concomitant formation of large surface dipoles between charged dopant ions and oppositely charged TMDs alters the vacuum level across the interface, contributing additionally to the work function modulation (Fig. 9a).[173]

Therefore, dopant molecules with a higher (lower) electronegativity/reduction potential than the flat band potential of n-type TMDs work as electron donors (acceptors) by donating (withdrawing) electrons to (from) the n-type TMD, which increases (decreases) the TMD electron carrier concentration; conversely, molecules with higher (lower) electronegativity than p-type TMDs withdraw (donate) electrons from (to) the p-type TMD, which depletes (accumulates) holes and thus decreases (increases) its hole carrier concentration. Fig. 9b summarizes several reductant (oxidant) agents enabling n-type (p-type) doping in TMDs.[20,139,174–183] For example, amorphous-TiO_{2-x} (chloride) doping significantly reduces the R_C and L_T of MoS_2 down to 180 (500) Ω μm and 15 (60) nm, respectively, which is one of the lowest R_C values reported to date, as a consequence of the substantial SB thinning induced by the heavy doping nearby the contact region.[67,184,185] Meanwhile, NO_2 chemisorption leads to degenerate p^+-WSe_2, thus enabling hole tunneling injection into p-WSe_2 through a narrower SB which enables ohmic contacts for the inspection of a high hole mobility of 250 $cm^2\ V^{-1}\ s^{-1}$, a SS of 60 mV dec^{-1} and an

Open Access Article. Published on 24 September 2018. Downloaded on 10/19/2018 10:38:30 AM.
This article is licensed under a Creative Commons Attribution-NonCommercial 3.0 Unported Licence.

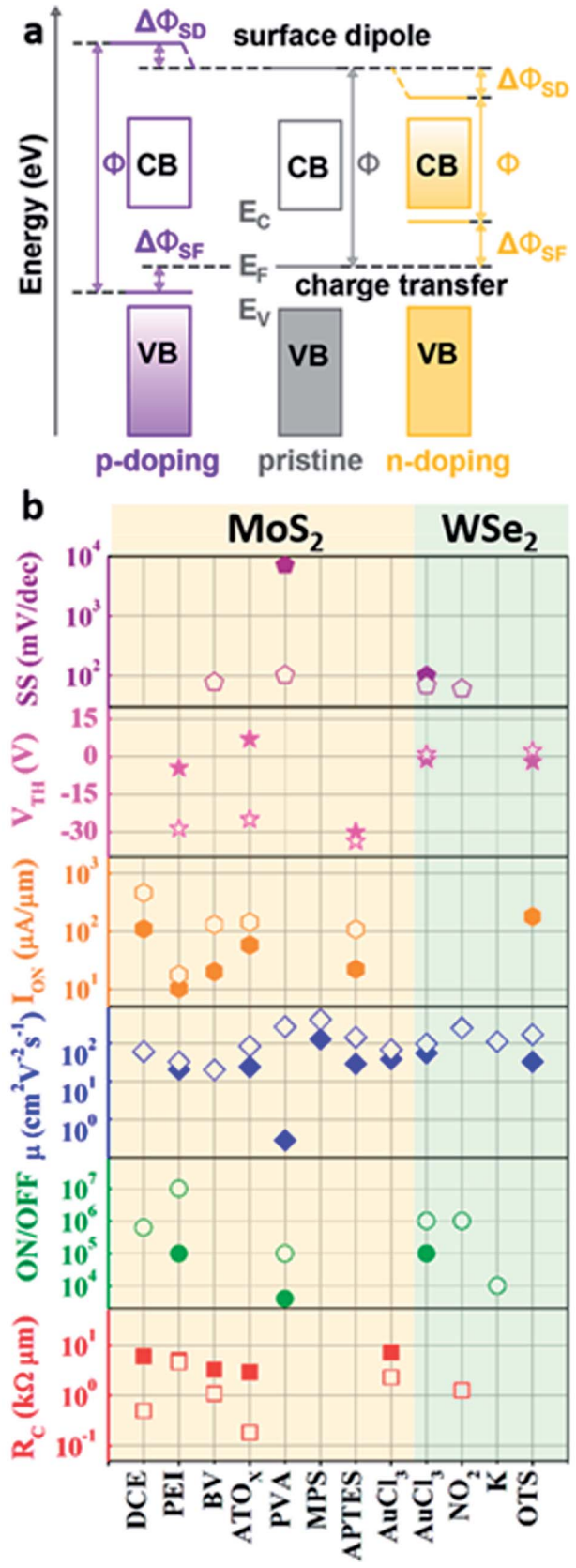

Fig. 9 (a) Schematic of the doping effect on the work function change ($\Delta\phi_f$) by emptying/filling states ($\Delta\phi_{SF}$) and creating surface dipoles ($\Delta\phi_{/SD}$).[173] (b) Electronic properties of MoS_2, and WSe_2 before (filled symbols) and after (empty symbols) chemical doping by different dopants: dichloroethane (DCE),[67] polyethyleneimine (PEI),[181] benzyl viologen (BV),[186] amorphous-TiO_{2-x} (ATO_x),[184] polyvinyl alcohol (PVA),[213] (3-mercaptopropyl)trimethoxysilane (MPS),[25] amino-propyltriethoxysilane (APTES),[214] gold chloride ($AuCl_3$),[78,158] (NO_2),[82] potassium (K),[215] and octadecyltrichlorosilane (OTS).[214] Reproduced with permission from ref. 173 © 2017, American Chemical Society.

enhanced on–off ratio.[82] Benzyl viologen can degenerate MoS_2 in the proximity of the metal contacts, leading to 3-fold R_C reduction and a SS of 77 mV dec^{-1}.[186] Furthermore, Au nanoparticle (NPs) decoration *via* $AuCl_3$ reduction on either n-MoS_2 or p-WSe_2 have shown p-type doping owing to the electron transfer from TMDs to high work function Au.[78,158,187,188] Indeed, increasing the $AuCl_3$ dopant concentration from 5 M to 20 M yields degenerate p-type doping in MoS_2, which has been used to devise CMOS inverters or nearly ideal rectifying pn diodes.[78,188]

3.8. Plasma engineering

Plasma treatment is a versatile tool to control the electronic properties of TMDs. For example, O_2 plasma exposure oxidizes MoS_2 by knocking off sulfur atoms and creating defects, thus leading to MoO_3. The higher work function of MoO_3 (6.9 eV) than MoS_2 (4.9 eV) creates a band offset between them; consequently, the interface between the exposed channel and the unexposed contacts forms a SB that acts as a tunneling barrier for electron injection.[189,190] Similarly, the O_2 plasma oxidizes p-WSe_2 into high work function WO_3 (6.7 eV), which improves the hole injection *via* SBH lowering, and thus reduces R_C and enhances mobility (Fig. 10a–c).[191] On the same line, selective contact area O_2 or Ar plasma exposure broadens the SBH distribution from 0.2–0.3 to 0.2–0.8 eV of MoS_2, thus degrading the electron mobility but enabling hole injection toward ambipolar transport.[192] Conversely, soft O_2, Ar, UV/ozone plasma treatments can repair structural defects, remove contaminants and passivate photo-excited traps, respectively, leading to enhanced mobility.[193–195] Alternatively, the H_2 plasma promotes the formation of sulfur vacancies, which act as a double-edged sword because they reduce contact resistance but at the same time increase the number of scattering centers that eventually reduce the mobility.[196] Additionally, contact-defect engineering by H_2 plasma treatment leads to air-stable degenerate n-WSe_2 with 2 orders of magnitude lower R_C compared to the pristine sample; consequently the on-current increases 20-fold and the SS reduces down to 66 mV dec^{-1}.[197]

3.9. Phase transformation engineering

Beyond the conventional 2H-semiconducting phase of TMD materials, there exist several polymorphic phases with intriguing states of matter such as 2D topological insulators, superconductors and Weyl semimetals.[198–200] Among them, the metallic phase characterized by V-shaped Dirac-Fermion like carriers, carrier concentrations higher than 10^{13} cm^{-2}, weak gate modulation and environmental stability can resolve the Schottky-limited transport in 2D-TMDs.[201] For instance, seven monolayer 1T-metallic phase TMD/metal structures have been

Open Access Article. Published on 24 September 2018. Downloaded on 10/19/2018 10:38:30 AM.
This article is licensed under a Creative Commons Attribution-NonCommercial 3.0 Unported Licence.

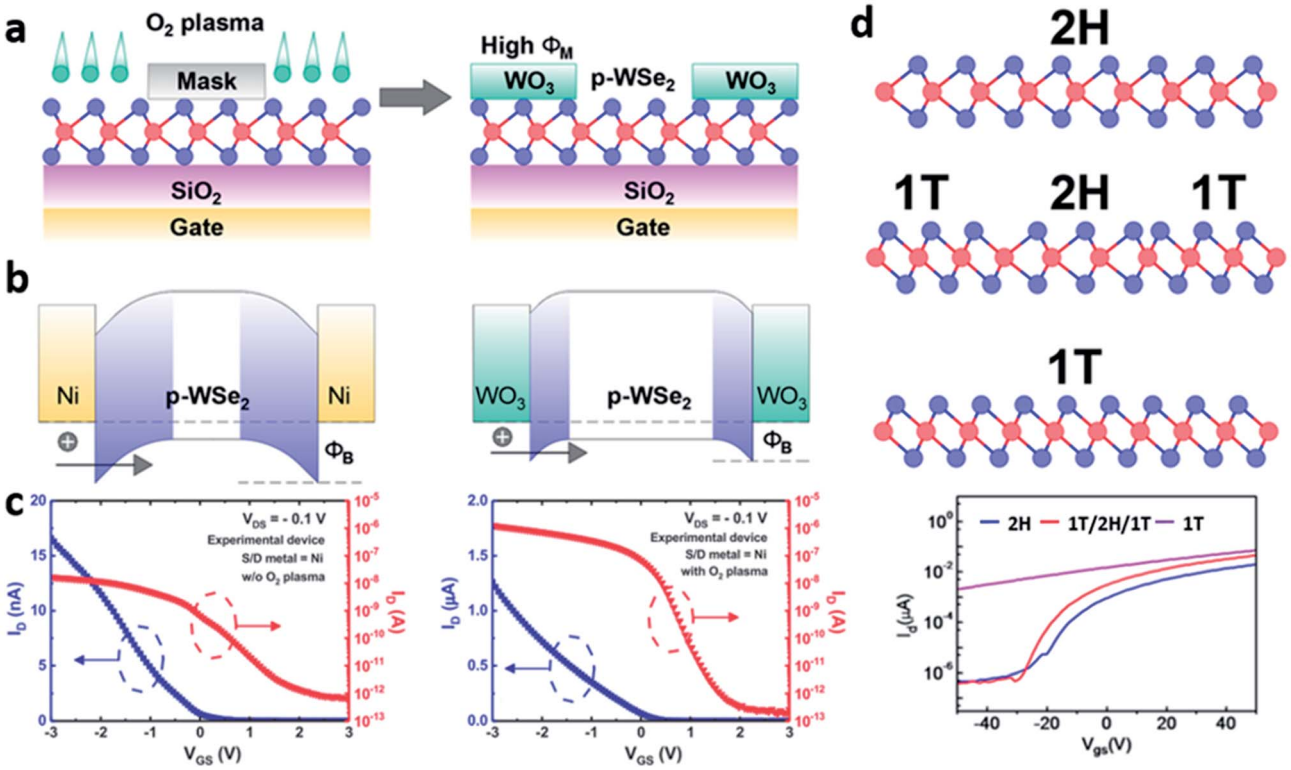

Fig. 10 Oxygen plasma exposure of WSe_2: (a) schematic showing the formation of WO_3 after O_2 plasma exposure, (b) improved hole injection *via* SB reduction due to the formation of high work function WO_3, and (c) transfer characteristics before and after oxygen plasma treatment.[191] (d) Schematic of devices based on the 2H to 1T phase transformation of MoS_2 by argon plasma and the corresponding transfer characteristics.[201] Reproduced with permission from ref. 191 © 2017, Elsevier; ref. 201 © 2017, American Chemical Society.

theoretically identified by Ouyang *et al.* as zero Schottky barrier contacts owing to efficient interface charge transfer based on the amount of interface orbital overlapping and lattice misfit.[202] Indeed, selective area semiconducting-to-metallic phase transformation exhibits defect-free atomically sharp interfaces and matched band alignment between the work function and the conduction band energy, leading to seamlessly ohmic side contacts with R_C as low as 200–300 Ω μm as well as improved device characteristics (Fig. 10d).[52,91,116,201,203,204] In addition, the metallic-1T phases of MoS_2, $MoTe_2$ and WSe_2 are stable up to 100, 300 and 180 °C respectively, although further thermal annealing or laser irradiation can reverse the transition back to the 2H-semiconducting phase.[203,205,206] Furthermore, experimental and theoretical calculations of sub-10 nm 1T/2H/1T MoS_2 structures exhibit an off-current of 10 pA μm^{-1}, an on–off ratio of 10^4–10^7, and a SS of 69–120 mV dec^{-1}, which are only limited by intraband tunneling at 3.3 nm.[91,207]

4. Conclusion, outlook and perspectives

This review summarizes the impact of the compelling properties of 2D-TMDs including chemical inertness, atomically thin nature, low DOS and large bandgaps on the carrier injection and transport towards high performance electronic devices. Although, the weak screening in 2D-TMDs enables fine carrier density modulation up to 10^{14} cm^{-2}, allowing metal-to-insulator transitions with optimized superconducting temperature, we emphasis that utmost care should be taken first on addressing the R_C, SB and FLP in order to achieve carrier injection with ohmic-contacts, and second on suppressing carrier traps and phonon scattering centers in order to achieve high mobility carrier transport towards ballistic transport in highly scaled devices.

To this extent, we survey several contact, dielectric and material engineering strategies involving surface and interface chemistry to optimize the charge injection and transport. The most successful strategies optimizing charge injection include graphene and BN 2D-interlayers, coplanar 2H-semiconducting/1T-metallic phase transitions, 1L-semiconducting/2L-metallic transitions in $PtSe_2$, and amorphous TiO_x capping layers; consequently, R_C can be reduced down to 300–70 Ω μm, which is in close proximity to the 100 Ω μm speculated by the ITRS roadmap. Furthermore, metal-transferred electrodes and alloyed 2D-metals not only provide low R_C ohmic contacts but also afford mobilities of 200–260 $cm^2 V^{-1} s^{-1}$ and on-currents of 320–660 μA μm^{-1}. On the other hand, the current transport can be readily tailored from degenerate doping to ambipolar transport by charge transfer *via* thiol-based self-assembled monolayers, $AuCl_3$ or potassium chemical doping, NO_2 gas exposure, and phosphor plasma among others. Furthermore, few-layer BN and Y_2O_3/HfO_2 stacked gate dielectrics can suppress phonon scattering and boost the mobility over 200

 This journal is © The Royal Society of Chemistry 2018

Open Access Article. Published on 24 September 2018. Downloaded on 10/19/2018 10:38:30 AM.
This article is licensed under a Creative Commons Attribution-NonCommercial 3.0 Unported Licence.

$cm^2 V^{-1} s^{-1}$ at RT, whereas, ionic electrolytes induce lowered SB *via* strong surface band bending, hence enabling tunneling currents that provide subthreshold swing slopes down to 60 mV dec^{-1}. Therefore, the remaining challenge for the next-generation of high performance electronic devices based on the unique properties of 2D-TMDs is to integrate the aforementioned strategies into large-scale and high-quality samples grown by either chemical-vapor-deposition techniques[208,209] or alternatively by solution processing methods,[210,211] which is certainly coming soon, but is not yet fully established.

Conflicts of interest

There are no conflicts to declare.

Acknowledgements

This work was financially supported by the King Abdullah University of Science and Technology (KAUST) Office of Sponsored Research (OSR-2016-CRG5-3005), KAUST Sensor Initiative, KAUST Solar Center, and KAUST baseline funding.

References

1 A. M. Ionescu and H. Riel, *Nature*, 2011, **479**, 329–337.
2 Y. Khatami and K. Banerjee, *IEEE Trans. Electron Devices*, 2009, **56**, 2752–2761.
3 Z. Qin, Z. Wei and A. Seabaugh, *IEEE Electron Device Lett.*, 2006, **27**, 297–300.
4 H. Lu and A. Seabaugh, *IEEE J. Electron Devices Soc.*, 2014, **2**, 44–49.
5 M. Si, C.-J. Su, C. Jiang, N. J. Conrad, H. Zhou, K. D. Maize, G. Qiu, C.-T. Wu, A. Shakouri, M. A. Alam and P. D. Ye, *Nat. Nanotechnol.*, 2018, **13**, 24–28.
6 F. A. McGuire, Z. Cheng, K. Price and A. D. Franklin, *Appl. Phys. Lett.*, 2016, **109**, 093101.
7 K. F. Mak, C. Lee, J. Hone, J. Shan and T. F. Heinz, *Phys. Rev. Lett.*, 2010, **105**, 136805.
8 K. S. Novoselov, D. Jiang, F. Schedin, T. J. Booth, V. V. Khotkevich, S. V. Morozov and A. K. Geim, *Proc. Natl. Acad. Sci. U. S. A.*, 2005, **102**, 10451–10453.
9 D. Lembke, S. Bertolazzi and A. Kis, *Acc. Chem. Res.*, 2015, **48**, 100–110.
10 B. Radisavljevic, A. Radenovic, J. Brivio, V. Giacometti and A. Kis, *Nat. Nanotechnol.*, 2011, **6**, 147–150.
11 A. K. Geim and I. V. Grigorieva, *Nature*, 2013, **499**, 419–425.
12 M. Chhowalla, H. S. Shin, G. Eda, L.-J. Li, K. P. Loh and H. Zhang, *Nat. Chem.*, 2013, **5**, 263.
13 A. H. Castro Neto, *Phys. Rev. Lett.*, 2001, **86**, 4382–4385.
14 H. Li, J. Wu, Z. Yin and H. Zhang, *Acc. Chem. Res.*, 2014, **47**, 1067–1075.
15 S. Mao, J. Chang, H. Pu, G. Lu, Q. He, H. Zhang and J. Chen, *Chem. Soc. Rev.*, 2017, **46**, 6872–6904.
16 R. Lv, J. A. Robinson, R. E. Schaak, D. Sun, Y. Sun, T. E. Mallouk and M. Terrones, *Acc. Chem. Res.*, 2015, **48**, 56–64.
17 D. Jariwala, V. K. Sangwan, L. J. Lauhon, T. J. Marks and M. C. Hersam, *ACS Nano*, 2014, **8**, 1102–1120.
18 H. Ilatikhameneh, Y. Tan, B. Novakovic, G. Klimeck, R. Rahman and J. Appenzeller, *IEEE Journal on Exploratory Solid-State Computational Devices and Circuits*, 2015, **1**, 12–18.
19 D. Sarkar, X. Xie, W. Liu, W. Cao, J. Kang, Y. Gong, S. Kraemer, P. M. Ajayan and K. Banerjee, *Nature*, 2015, **526**, 91–95.
20 H. Schmidt, F. Giustiniano and G. Eda, *Chem. Soc. Rev.*, 2015, **44**, 7715–7736.
21 Q. H. Wang, K. Kalantar-Zadeh, A. Kis, J. N. Coleman and M. S. Strano, *Nat. Nanotechnol.*, 2012, **7**, 699.
22 A. Allain, J. Kang, K. Banerjee and A. Kis, *Nat. Mater.*, 2015, **14**, 1195–1205.
23 S. Das, H. Y. Chen, A. V. Penumatcha and J. Appenzeller, *Nano Lett.*, 2013, **13**, 100–105.
24 C. Kim, I. Moon, D. Lee, M. S. Choi, F. Ahmed, S. Nam, Y. Cho, H. J. Shin, S. Park and W. J. Yoo, *ACS Nano*, 2017, **11**, 1588–1596.
25 Z. Yu, Y. Pan, Y. Shen, Z. Wang, Z. Y. Ong, T. Xu, R. Xin, L. Pan, B. Wang, L. Sun, J. Wang, G. Zhang, Y. W. Zhang, Y. Shi and X. Wang, *Nat. Commun.*, 2014, **5**, 5290.
26 X. Cui, G. H. Lee, Y. D. Kim, G. Arefe, P. Y. Huang, C. H. Lee, D. A. Chenet, X. Zhang, L. Wang, F. Ye, F. Pizzocchero, B. S. Jessen, K. Watanabe, T. Taniguchi, D. A. Muller, T. Low, P. Kim and J. Hone, *Nat. Nanotechnol.*, 2015, **10**, 534–540.
27 B. Radisavljevic and A. Kis, *Nat. Mater.*, 2013, **12**, 815–820.
28 W. Zhu, T. Low, Y. H. Lee, H. Wang, D. B. Farmer, J. Kong, F. Xia and P. Avouris, *Nat. Commun.*, 2014, **5**, 3087.
29 S.-L. Li, K. Wakabayashi, Y. Xu, S. Nakaharai, K. Komatsu, W.-W. Li, Y.-F. Lin, A. Aparecido-Ferreira and K. Tsukagoshi, *Nano Lett.*, 2013, **13**, 3546–3552.
30 Z. Yu, Z. Y. Ong, Y. Pan, Y. Cui, R. Xin, Y. Shi, B. Wang, Y. Wu, T. Chen, Y. W. Zhang, G. Zhang and X. Wang, *Adv. Mater.*, 2016, **28**, 547–552.
31 S.-L. Li, K. Tsukagoshi, E. Orgiu and P. Samori, *Chem. Soc. Rev.*, 2016, **45**, 118–151.
32 X. Zou, J. Wang, C. H. Chiu, Y. Wu, X. Xiao, C. Jiang, W. W. Wu, L. Mai, T. Chen, J. Li, J. C. Ho and L. Liao, *Adv. Mater.*, 2014, **26**, 6255–6261.
33 Y. Liu, P. Stradins and S.-H. Wei, *Sci. Adv.*, 2016, **2**(4), e1600069.
34 Y. Guo, D. Liu and J. Robertson, *Appl. Phys. Lett.*, 2015, **106**, 173106.
35 J. R. Chen, P. M. Odenthal, A. G. Swartz, G. C. Floyd, H. Wen, K. Y. Luo and R. K. Kawakami, *Nano Lett.*, 2013, **13**, 3106–3110.
36 P. Dharmaraj, P. J. Jesuraj and K. Jeganathan, *Appl. Phys. Lett.*, 2016, **108**, 051605.
37 J. Kang, W. Liu, D. Sarkar, D. Jena and K. Banerjee, *Phys. Rev. X*, 2014, **4**, 031005.
38 C. Gong, L. Colombo, R. M. Wallace and K. Cho, *Nano Lett.*, 2014, **14**, 1714–1720.
39 M. Farmanbar and G. Brocks, *Phys. Rev. B: Condens. Matter Mater. Phys.*, 2015, **91**, 161304(R).

Open Access Article. Published on 24 September 2018. Downloaded on 10/19/2018 10:38:30 AM.
This article is licensed under a Creative Commons Attribution-NonCommercial 3.0 Unported Licence.

40 Y. Liu, J. Guo, E. Zhu, L. Liao, S.-J. Lee, M. Ding, I. Shakir, V. Gambin, Y. Huang and X. Duan, *Nature*, 2018, **557**, 696–700.
41 S.-L. Li, K. Komatsu, S. Nakaharai, Y.-F. Lin, M. Yamamoto, X. Duan and K. Tsukagoshi, *ACS Nano*, 2014, **8**, 12836–12842.
42 C. J. L. de la Rosa, G. Arutchelvan, I. Radu, D. Lin, C. Huyghebaert, M. Heyns and S. De Gendt, *ECS J. Solid State Sci. Technol.*, 2016, **5**, Q3072–Q3081.
43 Y. Yoon, K. Ganapathi and S. Salahuddin, *Nano Lett.*, 2011, **11**, 3768–3773.
44 T. Roy, M. Tosun, J. S. Kang, A. B. Sachid, S. B. Desai, M. Hettick, C. C. Hu and A. Javey, *ACS Nano*, 2014, **8**, 6259–6264.
45 K. Nagashio, T. Nishimura, K. Kita and A. Toriumi, *Appl. Phys. Lett.*, 2010, **97**, 143514.
46 Y. Guo, Y. Han, J. Li, A. Xiang, X. Wei, S. Gao and Q. Chen, *ACS Nano*, 2014, **8**, 7771–7779.
47 H. Liu, M. Si, Y. Deng, A. T. Neal, Y. Du, S. Najmaei, P. M. Ajayan, J. Lou and P. D. Ye, *ACS Nano*, 2014, **8**, 1031–1038.
48 H. Yuan, G. Cheng, S. Yu, A. R. H. Walker, C. A. Richter, M. Pan and Q. Li, *Appl. Phys. Lett.*, 2016, **108**, 103505.
49 D. Somvanshi, S. Kallatt, C. Venkatesh, S. Nair, G. Gupta, J. K. Anthony, D. Karmakar and K. Majumdar, *Phys. Rev. B*, 2017, **96**, 205423.
50 X. Cui, E.-M. Shih, L. A. Jauregui, S. H. Chae, Y. D. Kim, B. Li, D. Seo, K. Pistunova, J. Yin, J.-H. Park, H.-J. Choi, Y. H. Lee, K. Watanabe, T. Taniguchi, P. Kim, C. R. Dean and J. C. Hone, *Nano Lett.*, 2017, **17**, 4781–4786.
51 H.-Y. Chang, W. Zhu and D. Akinwande, *Appl. Phys. Lett.*, 2014, **104**, 113504.
52 Y. Katagiri, T. Nakamura, A. Ishii, C. Ohata, M. Hasegawa, S. Katsumoto, T. Cusati, A. Fortunelli, G. Iannaccone, G. Fiori, S. Roche and J. Haruyama, *Nano Lett.*, 2016, **16**, 3788–3794.
53 A. Anwar, B. Nabet, J. Culp and F. Castro, *J. Appl. Phys.*, 1999, **85**, 2663–2666.
54 D. K. Schroder, *Semiconductor Material and Device Characterization*, Wiley-Interscience, 2006.
55 F. Zahid, L. Liu, Y. Zhu, J. Wang and H. Guo, *AIP Adv.*, 2013, **3**, 052111.
56 D. Qiu and E. K. Kim, *Sci. Rep.*, 2015, **5**, 13743.
57 W. Wang, Y. Liu, L. Tang, Y. Jin, T. Zhao and F. Xiu, *Sci. Rep.*, 2014, **4**, 6928.
58 S. Das, A. Prakash, R. Salazar and J. Appenzeller, *ACS Nano*, 2014, **8**, 1681–1689.
59 F. Ahmed, M. S. Choi, X. Liu and W. J. Yoo, *Nanoscale*, 2015, **7**, 9222–9228.
60 H.-M. Li, D. Lee, D. Qu, X. Liu, J. Ryu, A. Seabaugh and W. J. Yoo, *Nat. Commun.*, 2015, **6**, 6564.
61 J. Appenzeller, M. Radosavljević, J. Knoch and P. Avouris, *Phys. Rev. Lett.*, 2004, **92**, 048301.
62 N. R. Pradhan, D. Rhodes, S. Memaran, J. M. Poumirol, D. Smirnov, S. Talapatra, S. Feng, N. Perea-Lopez, A. L. Elias, M. Terrones, P. M. Ajayan and L. Balicas, *Sci. Rep.*, 2015, **5**, 8979.
63 A. Dankert, L. Langouche, M. V. Kamalakar and S. P. Dash, *ACS Nano*, 2014, **8**, 476–482.
64 H. J. Chuang, X. Tan, N. J. Ghimire, M. M. Perera, B. Chamlagain, M. M. Cheng, J. Yan, D. Mandrus, D. Tomanek and Z. Zhou, *Nano Lett.*, 2014, **14**, 3594–3601.
65 M. Nan and J. Debdeep, *2D Mater.*, 2015, **2**, 015003.
66 D. Jiménez, *Appl. Phys. Lett.*, 2012, **101**, 243501.
67 L. Yang, K. Majumdar, H. Liu, Y. Du, H. Wu, M. Hatzistergos, P. Y. Hung, R. Tieckelmann, W. Tsai, C. Hobbs and P. D. Ye, *Nano Lett.*, 2014, **14**, 6275–6280.
68 S. Das and J. Appenzeller, *Nano Lett.*, 2013, **13**, 3396–3402.
69 N. Ma and D. Jena, *Phys. Rev. X*, 2014, **4**, 011043.
70 J. Wu, H. Schmidt, K. K. Amara, X. Xu, G. Eda and B. Ozyilmaz, *Nano Lett.*, 2014, **14**, 2730–2734.
71 D. Jariwala, V. K. Sangwan, D. J. Late, J. E. Johns, V. P. Dravid, T. J. Marks, L. J. Lauhon and M. C. Hersam, *Appl. Phys. Lett.*, 2013, **102**, 173107.
72 S. Ghatak, A. N. Pal and A. Ghosh, *ACS Nano*, 2011, **5**, 7707–7712.
73 X. Chen, Z. Wu, S. Xu, L. Wang, R. Huang, Y. Han, W. Ye, W. Xiong, T. Han, G. Long, Y. Wang, Y. He, Y. Cai, P. Sheng and N. Wang, *Nat. Commun.*, 2015, **6**, 6088.
74 S. Das and J. Appenzeller, *Phys. Status Solidi RRL*, 2013, **7**, 268–273.
75 B. W. Baugher, H. O. Churchill, Y. Yang and P. Jarillo-Herrero, *Nano Lett.*, 2013, **13**, 4212–4216.
76 W. Huang, X. Luo, C. K. Gan, S. Y. Quek and G. Liang, *Phys. Chem. Chem. Phys.*, 2014, **16**, 10866–10874.
77 W. Huang, H. Da and G. Liang, *J. Appl. Phys.*, 2013, **113**, 104304.
78 X. Liu, D. Qu, J. Ryu, F. Ahmed, Z. Yang, D. Lee and W. J. Yoo, *Adv. Mater.*, 2016, **28**, 2345–2351.
79 D. Ovchinnikov, A. Allain, Y.-S. Huang, D. Dumcenco and A. Kis, *ACS Nano*, 2014, **8**, 8174–8181.
80 K. Kaasbjerg, K. S. Thygesen and K. W. Jacobsen, *Phys. Rev. B: Condens. Matter Mater. Phys.*, 2012, **85**, 115317.
81 H. Wang, L. Yu, Y. H. Lee, W. Fang, A. Hsu, P. Herring, M. Chin, M. Dubey, L. J. Li, J. Kong and T. Palacios, *presented in part at the 2012 International Electron Devices Meeting*, 10-13 Dec. 2012.
82 H. Fang, S. Chuang, T. C. Chang, K. Takei, T. Takahashi and A. Javey, *Nano Lett.*, 2012, **12**, 3788–3792.
83 S. Kim, A. Konar, W.-S. Hwang, J. H. Lee, J. Lee, J. Yang, C. Jung, H. Kim, J.-B. Yoo, J.-Y. Choi, Y. W. Jin, S. Y. Lee, D. Jena, W. Choi and K. Kim, *Nat. Commun.*, 2012, **3**, 1011.
84 H. Qiu, T. Xu, Z. Wang, W. Ren, H. Nan, Z. Ni, Q. Chen, S. Yuan, F. Miao, F. Song, G. Long, Y. Shi, L. Sun, J. Wang and X. Wang, *Nat. Commun.*, 2013, **4**, 2642.
85 F. W. Van Keuls, X. L. Hu, H. W. Jiang and A. J. Dahm, *Phys. Rev. B: Condens. Matter Mater. Phys.*, 1997, **56**, 1161–1169.
86 L. Wang, Y. Li, X. Gong, A. V.-Y. Thean and G. Liang, *IEEE Electron Device Lett.*, 2018, **39**, 761–764.
87 L. Wang, Y. Li, X. Feng, K. W. Ang, X. Gong, A. Thean and G. Liang, *presented in part at the 2017 IEEE International Electron Devices Meeting (IEDM)*, 2-6 Dec. 2017.
88 B. Liu, A. Abbas and C. Zhou, *Adv. Electron. Mater.*, 2017, **3**, 1700045.

 This journal is © The Royal Society of Chemistry 2018

Open Access Article. Published on 24 September 2018. Downloaded on 10/19/2018 10:38:30 AM.
This article is licensed under a Creative Commons Attribution-NonCommercial 3.0 Unported Licence.

89 S. V. Suryavanshi and E. Pop, *J. Appl. Phys.*, 2016, **120**, 224503.
90 H. Nam, S. Wi, H. Rokni, M. Chen, G. Priessnitz, W. Lu and X. Liang, *ACS Nano*, 2013, **7**, 5870–5881.
91 A. Nourbakhsh, A. Zubair, R. N. Sajjad, A. K. G. Tavakkoli, W. Chen, S. Fang, X. Ling, J. Kong, M. S. Dresselhaus, E. Kaxiras, K. K. Berggren, D. Antoniadis and T. Palacios, *Nano Lett.*, 2016, **16**, 7798–7806.
92 M. S. Fuhrer and J. Hone, *Nat. Nanotechnol.*, 2013, **8**, 146.
93 D. Jena, K. Banerjee and G. H. Xing, *Nat. Mater.*, 2014, **13**, 1076.
94 J. Chang, L. F. Register and S. K. Banerjee, *presented in part at the 2013 International Conference on Simulation of Semiconductor Processes and Devices (SISPAD)*, 3-5 Sept. 2013.
95 X.-W. Jiang and S.-S. Li, *Appl. Phys. Lett.*, 2014, **104**, 193510.
96 J. Chang, L. F. Register and S. K. Banerjee, *Appl. Phys. Lett.*, 2013, **103**, 223509.
97 L. Liu, Y. Lu and J. Guo, *IEEE Trans. Electron Devices*, 2013, **60**, 4133–4139.
98 K. L. Low, W. Huang, Y. C. Yeo and G. Liang, *IEEE Trans. Electron Devices*, 2014, **61**, 1590–1598.
99 A. Nourbakhsh, A. Zubair, S. Huang, X. Ling, M. S. Dresselhaus, J. Kong, S. D. Gendt and T. Palacios, *presented in part at the 2015 Symposium on VLSI Technology (VLSI Technology)*, 16-18 June 2015.
100 C. D. English, K. K. H. Smithe, R. L. Xu and E. Pop, *presented in part at the 2016 IEEE International Electron Devices Meeting (IEDM)*, 3-7 Dec. 2016.
101 S. B. Desai, S. R. Madhvapathy, A. B. Sachid, J. P. Llinas, Q. Wang, G. H. Ahn, G. Pitner, M. J. Kim, J. Bokor, C. Hu, H.-S. P. Wong and A. Javey, *Science*, 2016, **354**, 99–102.
102 J. I. J. Wang, Y. Yang, Y.-A. Chen, K. Watanabe, T. Taniguchi, H. O. H. Churchill and P. Jarillo-Herrero, *Nano Lett.*, 2015, **15**, 1898–1903.
103 H.-J. Chuang, B. Chamlagain, M. Koehler, M. M. Perera, J. Yan, D. Mandrus, D. Tománek and Z. Zhou, *Nano Lett.*, 2016, **16**, 1896–1902.
104 A. R. Kim, Y. Kim, J. Nam, H.-S. Chung, D. J. Kim, J.-D. Kwon, S. W. Park, J. Park, S. Y. Choi, B. H. Lee, J. H. Park, K. H. Lee, D.-H. Kim, S. M. Choi, P. M. Ajayan, M. G. Hahm and B. Cho, *Nano Lett.*, 2016, **16**, 1890–1895.
105 Y. Du, L. Yang, J. Zhang, H. Liu, K. Majumdar, P. D. Kirsch and P. D. Ye, *IEEE Electron Device Lett.*, 2014, **35**, 599–601.
106 H. Yu, A. Kutana and B. I. Yakobson, *Nano Lett.*, 2016, **16**, 5032–5036.
107 X. Ling, Y. Lin, Q. Ma, Z. Wang, Y. Song, L. Yu, S. Huang, W. Fang, X. Zhang, A. L. Hsu, Y. Bie, Y.-H. Lee, Y. Zhu, L. Wu, J. Li, P. Jarillo-Herrero, M. Dresselhaus, T. Palacios and J. Kong, *Adv. Mater.*, 2016, **28**, 2322–2329.
108 M. Zhao, Y. Ye, Y. Han, Y. Xia, H. Zhu, S. Wang, Y. Wang, D. A. Muller and X. Zhang, *Nat. Nanotechnol.*, 2016, **11**, 954.
109 H.-L. Tang, M.-H. Chiu, C.-C. Tseng, S.-H. Yang, K.-J. Hou, S.-Y. Wei, J.-K. Huang, Y.-F. Lin, C.-H. Lien and L.-J. Li, *ACS Nano*, 2017, **11**, 12817–12823.
110 M. H. D. Guimarães, H. Gao, Y. Han, K. Kang, S. Xie, C.-J. Kim, D. A. Muller, D. C. Ralph and J. Park, *ACS Nano*, 2016, **10**, 6392–6399.
111 Y. Kim, A. R. Kim, J. H. Yang, K. E. Chang, J.-D. Kwon, S. Y. Choi, J. Park, K. E. Lee, D.-H. Kim, S. M. Choi, K. H. Lee, B. H. Lee, M. G. Hahm and B. Cho, *Nano Lett.*, 2016, **16**, 5928–5933.
112 M. Tosun, S. Chuang, H. Fang, A. B. Sachid, M. Hettick, Y. Lin, Y. Zeng and A. Javey, *ACS Nano*, 2014, **8**, 4948–4953.
113 A. Nipane, D. Karmakar, N. Kaushik, S. Karande and S. Lodha, *ACS Nano*, 2016, **10**, 2128–2137.
114 M.-Y. Li, Y. Shi, C.-C. Cheng, L.-S. Lu, Y.-C. Lin, H.-L. Tang, M.-L. Tsai, C.-W. Chu, K.-H. Wei, J.-H. He, W.-H. Chang, K. Suenaga and L.-J. Li, *Science*, 2015, **349**, 524–528.
115 M.-L. Tsai, M.-Y. Li, J. R. D. Retamal, K.-T. Lam, Y.-C. Lin, K. Suenaga, L.-J. Chen, G. Liang, L.-J. Li and J.-H. He, *Adv. Mater.*, 2017, **29**, 1701168.
116 R. Kappera, D. Voiry, S. E. Yalcin, B. Branch, G. Gupta, A. D. Mohite and M. Chhowalla, *Nat. Mater.*, 2014, **13**, 1128.
117 M. Ghorbani-Asl, A. Kuc, P. Miró and T. Heine, *Adv. Mater.*, 2016, **28**, 853–856.
118 Y. Wang, L. Li, W. Yao, S. Song, J. T. Sun, J. Pan, X. Ren, C. Li, E. Okunishi, Y.-Q. Wang, E. Wang, Y. Shao, Y. Y. Zhang, H.-t. Yang, E. F. Schwier, H. Iwasawa, K. Shimada, M. Taniguchi, Z. Cheng, S. Zhou, S. Du, S. J. Pennycook, S. T. Pantelides and H.-J. Gao, *Nano Lett.*, 2015, **15**, 4013–4018.
119 A. Ciarrocchi, A. Avsar, D. Ovchinnikov and A. Kis, *Nat. Commun.*, 2018, **9**, 919.
120 X.-W. Jiang, J. Gong, N. Xu, S.-S. Li, J. Zhang, Y. Hao and L.-W. Wang, *Appl. Phys. Lett.*, 2014, **104**, 023512.
121 S. McDonnell, R. Addou, C. Buie, R. M. Wallace and C. L. Hinkle, *ACS Nano*, 2014, **8**, 2880–2888.
122 W. Liu, J. Kang, D. Sarkar, Y. Khatami, D. Jena and K. Banerjee, *Nano Lett.*, 2013, **13**, 1983–1990.
123 M. Fontana, T. Deppe, A. K. Boyd, M. Rinzan, A. Y. Liu, M. Paranjape and P. Barbara, *Sci. Rep.*, 2013, **3**, 1634.
124 W. S. Leong, X. Luo, Y. Li, K. H. Khoo, S. Y. Quek and J. T. L. Thong, *ACS Nano*, 2015, **9**, 869–877.
125 M. Abraham and S. E. Mohney, *J. Appl. Phys.*, 2017, **122**, 115306.
126 C. D. English, G. Shine, V. E. Dorgan, K. C. Saraswat and E. Pop, *Nano Lett.*, 2016, **16**, 3824–3830.
127 C. M. Smyth, R. Addou, S. McDonnell, C. L. Hinkle and R. M. Wallace, *J. Phys. Chem. C*, 2016, **120**, 14719–14729.
128 X.-X. Li, Z.-Q. Fan, P.-Z. Liu, M.-L. Chen, X. Liu, C.-K. Jia, D.-M. Sun, X.-W. Jiang, Z. Han, V. Bouchiat, J.-J. Guo, J.-H. Chen and Z.-D. Zhang, *Nat. Commun.*, 2017, **8**, 970.
129 S. Chuang, C. Battaglia, A. Azcatl, S. McDonnell, J. S. Kang, X. Yin, M. Tosun, R. Kapadia, H. Fang, R. M. Wallace and A. Javey, *Nano Lett.*, 2014, **14**, 1337–1342.
130 J. H. Choi, H. K. Jang, J. E. Jin, J. M. Shin, D. H. Kim and G. T. Kim, *Appl. Phys. Lett.*, 2016, **109**, 183102.
131 W. Park, Y. Kim, L. Sang Kyung, U. Jung, Y. Jin Ho, C. Cho, K. Yun Ji, L. Sung Kwan, H. In Seol, H. B. R. Lee and L. Byoung Hun, *presented in part at the 2014 IEEE International Electron Devices Meeting*, 15-17 Dec. 2014.
132 N. Kaushik, D. Karmakar, A. Nipane, S. Karande and S. Lodha, *ACS Appl. Mater. Interfaces*, 2016, **8**, 256–263.
133 D. Fu, J. Zhou, S. Tongay, K. Liu, W. Fan, T.-J. K. Liu and J. Wu, *Appl. Phys. Lett.*, 2013, **103**, 183105.

Open Access Article. Published on 24 September 2018. Downloaded on 10/19/2018 10:38:30 AM.
This article is licensed under a Creative Commons Attribution-NonCommercial 3.0 Unported Licence.

134 G.-A. Mahdi, D. B. Paul, K. Koziol, H. Thomas and K. Agnieszka, *2D Mater.*, 2016, **3**, 025018.
135 C.-Y. Chen, J. R. D. Retamal, I. W. Wu, D.-H. Lien, M.-W. Chen, Y. Ding, Y.-L. Chueh, C.-I. Wu and J.-H. He, *ACS Nano*, 2012, **6**, 9366–9372.
136 C.-Y. Chen, M.-W. Chen, J.-J. Ke, C.-A. Lin, J. R. D. Retamal and J.-H. He, *Pure Appl. Chem.*, 2010, **82**(11), 2055–2073.
137 J. R. D. Retamal, C.-Y. Chen, D.-H. Lien, M. R. S. Huang, C.-A. Lin, C.-P. Liu and J.-H. He, *ACS Photonics*, 2014, **1**, 354–359.
138 S. Y. Lee, U. J. Kim, J. Chung, H. Nam, H. Y. Jeong, G. H. Han, H. Kim, H. M. Oh, H. Lee, H. Kim, Y. G. Roh, J. Kim, S. W. Hwang, Y. Park and Y. H. Lee, *ACS Nano*, 2016, **10**, 6100–6107.
139 S. Tongay, J. Zhou, C. Ataca, J. Liu, J. S. Kang, T. S. Matthews, L. You, J. Li, J. C. Grossman and J. Wu, *Nano Lett.*, 2013, **13**, 2831–2836.
140 H. Qiu, L. Pan, Z. Yao, J. Li, Y. Shi and X. Wang, *Appl. Phys. Lett.*, 2012, **100**, 123104.
141 L. Qi, Y. Wang, L. Shen and Y. Wu, *Appl. Phys. Lett.*, 2016, **108**, 063103.
142 H.-P. Komsa, J. Kotakoski, S. Kurasch, O. Lehtinen, U. Kaiser and A. V. Krasheninnikov, *Phys. Rev. Lett.*, 2012, **109**, 035503.
143 G.-A. Mahdi, K. Silvan, E. S. Douglas and V. K. Arkady, *2D Mater.*, 2017, **4**, 025078.
144 I. Yury Yu, R. Gerhard, W. Michael, K. Theresia, G. Alexander, M. F. Marco, M. Thomas and G. Tibor, *2D Mater.*, 2016, **3**, 035004.
145 K. Dolui, I. Rungger and S. Sanvito, *Phys. Rev. B: Condens. Matter Mater. Phys.*, 2013, **87**, 165402.
146 W. Bao, X. Cai, D. Kim, K. Sridhara and M. S. Fuhrer, *Appl. Phys. Lett.*, 2013, **102**, 042104.
147 P. Bolshakov, P. Zhao, A. Azcatl, P. K. Hurley, R. M. Wallace and C. D. Young, *Microelectron. Eng.*, 2017, **178**, 190–193.
148 H. Liu and P. D. Ye, *IEEE Electron Device Lett.*, 2012, **33**, 546–548.
149 H. C. P. Movva, A. Rai, S. Kang, K. Kim, B. Fallahazad, T. Taniguchi, K. Watanabe, E. Tutuc and S. K. Banerjee, *ACS Nano*, 2015, **9**, 10402–10410.
150 M. W. Iqbal, M. Z. Iqbal, M. F. Khan, M. A. Shehzad, Y. Seo, J. H. Park, C. Hwang and J. Eom, *Sci. Rep.*, 2015, **5**, 10699.
151 G.-H. Lee, X. Cui, Y. D. Kim, G. Arefe, X. Zhang, C.-H. Lee, F. Ye, K. Watanabe, T. Taniguchi, P. Kim and J. Hone, *ACS Nano*, 2015, **9**, 7019–7026.
152 M. M. Perera, M.-W. Lin, H.-J. Chuang, B. P. Chamlagain, C. Wang, X. Tan, M. M.-C. Cheng, D. Tománek and Z. Zhou, *ACS Nano*, 2013, **7**, 4449–4458.
153 L. Ming-Wei, L. Lezhang, L. Qing, T. Xuebin, S. D. Kulwinder, Z. Peng, M. N. Vaman, C. Mark Ming-Cheng and Z. Zhixian, *J. Phys. D: Appl. Phys.*, 2012, **45**, 345102.
154 M. R. Tchalala, J. K. El-Demellawi, E. Abou-Hamad, J. R. D. Retamal, P. Varadhan, J.-H. He and S. Chaieb, *Appl. Mater. Today*, 2017, **9**, 10–20.
155 W. Shi, J. Ye, Y. Zhang, R. Suzuki, M. Yoshida, J. Miyazaki, N. Inoue, Y. Saito and Y. Iwasa, *Sci. Rep.*, 2015, **5**, 12534.
156 J. T. Ye, Y. J. Zhang, R. Akashi, M. S. Bahramy, R. Arita and Y. Iwasa, *Science*, 2012, **338**, 1193–1196.
157 D. Braga, I. Gutierrez Lezama, H. Berger and A. F. Morpurgo, *Nano Lett.*, 2012, **12**, 5218–5223.
158 C.-H. Chen, C.-L. Wu, J. Pu, M.-H. Chiu, P. Kumar, T. Takenobu and L.-J. Li, *2D Mater.*, 2014, **1**, 034001.
159 S. Jo, N. Ubrig, H. Berger, A. B. Kuzmenko and A. F. Morpurgo, *Nano Lett.*, 2014, **14**, 2019–2025.
160 Y. J. Zhang, J. T. Ye, Y. Yomogida, T. Takenobu and Y. Iwasa, *Nano Lett.*, 2013, **13**, 3023–3028.
161 Y. J. Zhang, T. Oka, R. Suzuki, J. T. Ye and Y. Iwasa, *Science*, 2014, **344**, 725–728.
162 H. Yuan, M. S. Bahramy, K. Morimoto, S. Wu, K. Nomura, B.-J. Yang, H. Shimotani, R. Suzuki, M. Toh, C. Kloc, X. Xu, R. Arita, N. Nagaosa and Y. Iwasa, *Nat. Phys.*, 2013, **9**, 563.
163 A. Pospischil, M. M. Furchi and T. Mueller, *Nat. Nanotechnol.*, 2014, **9**, 257.
164 D. J. Groenendijk, M. Buscema, G. A. Steele, S. Michaelis de Vasconcellos, R. Bratschitsch, H. S. J. van der Zant and A. Castellanos-Gomez, *Nano Lett.*, 2014, **14**, 5846–5852.
165 B. W. H. Baugher, H. O. H. Churchill, Y. Yang and P. Jarillo-Herrero, *Nat. Nanotechnol.*, 2014, **9**, 262.
166 Y.-Q. Bie, G. Grosso, M. Heuck, M. M. Furchi, Y. Cao, J. Zheng, D. Bunandar, E. Navarro-Moratalla, L. Zhou, D. K. Efetov, T. Taniguchi, K. Watanabe, J. Kong, D. Englund and P. Jarillo-Herrero, *Nat. Nanotechnol.*, 2017, **12**, 1124.
167 J. S. Ross, P. Klement, A. M. Jones, N. J. Ghimire, J. Yan, D. G. Mandrus, T. Taniguchi, K. Watanabe, K. Kitamura, W. Yao, D. H. Cobden and X. Xu, *Nat. Nanotechnol.*, 2014, **9**, 268–272.
168 M. R. Laskar, D. N. Nath, L. Ma, E. W. L. II, C. H. Lee, T. Kent, Z. Yang, R. Mishra, M. A. Roldan, J.-C. Idrobo, S. T. Pantelides, S. J. Pennycook, R. C. Myers, Y. Wu and S. Rajan, *Appl. Phys. Lett.*, 2014, **104**, 092104.
169 J. Suh, T. E. Park, D. Y. Lin, D. Fu, J. Park, H. J. Jung, Y. Chen, C. Ko, C. Jang, Y. Sun, R. Sinclair, J. Chang, S. Tongay and J. Wu, *Nano Lett.*, 2014, **14**, 6976–6982.
170 Y. Fu, M. Long, A. Gao, Y. Wang, C. Pan, X. Liu, J. Zeng, K. Xu, L. Zhang, E. Liu, W. Hu, X. Wang and F. Miao, *Appl. Phys. Lett.*, 2017, **111**, 043502.
171 H. S. Smalo, P. O. Astrand and S. Ingebrigtsen, *IEEE Trans. Dielectr. Electr. Insul.*, 2010, **17**, 733–741.
172 J. Kang, S. Tongay, J. Zhou, J. Li and J. Wu, *Appl. Phys. Lett.*, 2013, **102**, 012111.
173 M.-Y. Tsai, S. Zhang, P. M. Campbell, R. R. Dasari, X. Ba, A. Tarasov, S. Graham, S. Barlow, S. R. Marder and E. M. Vogel, *Chem. Mater.*, 2017, **29**, 7296–7304.
174 S. Mouri, Y. Miyauchi and K. Matsuda, *Nano Lett.*, 2013, **13**, 5944–5948.
175 D.-H. Kang, S. R. Dugasani, H.-Y. Park, J. Shim, B. Gnapareddy, J. Jeon, S. Lee, Y. Roh, S. H. Park and J.-H. Park, *Sci. Rep.*, 2016, **6**, 20333.
176 J. D. Lin, C. Han, F. Wang, R. Wang, D. Xiang, S. Qin, X.-A. Zhang, L. Wang, H. Zhang, A. T. S. Wee and W. Chen, *ACS Nano*, 2014, **8**, 5323–5329.

 This journal is © The Royal Society of Chemistry 2018

Open Access Article. Published on 24 September 2018. Downloaded on 10/19/2018 10:38:30 AM.
This article is licensed under a Creative Commons Attribution-NonCommercial 3.0 Unported Licence.

177 H.-Y. Park, S. R. Dugasani, D.-H. Kang, J. Jeon, S. K. Jang, S. Lee, Y. Roh, S. H. Park and J.-H. Park, *ACS Nano*, 2014, **8**, 11603–11613.
178 B. Liu, L. Chen, G. Liu, A. N. Abbas, M. Fathi and C. Zhou, *ACS Nano*, 2014, **8**, 5304–5314.
179 S. Dey, H. S. S. R. Matte, S. N. Shirodkar, U. V. Waghmare and C. N. R. Rao, *Chem.–Asian J.*, 2013, **8**, 1780–1784.
180 F. K. Perkins, A. L. Friedman, E. Cobas, P. M. Campbell, G. G. Jernigan and B. T. Jonker, *Nano Lett.*, 2013, **13**, 668–673.
181 Y. Du, H. Liu, A. T. Neal, M. Si and P. D. Ye, *IEEE Electron Device Lett.*, 2013, **34**, 1328–1330.
182 H. Nan, Z. Wang, W. Wang, Z. Liang, Y. Lu, Q. Chen, D. He, P. Tan, F. Miao, X. Wang, J. Wang and Z. Ni, *ACS Nano*, 2014, **8**, 5738–5745.
183 H. Li, Z. Yin, Q. He, H. Li, X. Huang, G. Lu, D. W. H. Fam, A. I. Y. Tok, Q. Zhang and H. Zhang, *Small*, 2012, **8**, 63–67.
184 A. Rai, A. Valsaraj, H. C. Movva, A. Roy, R. Ghosh, S. Sonde, S. Kang, J. Chang, T. Trivedi, R. Dey, S. Guchhait, S. Larentis, L. F. Register, E. Tutuc and S. K. Banerjee, *Nano Lett.*, 2015, **15**, 4329–4336.
185 Y. Lingming, K. Majumdar, Y. Du, H. Liu, W. Heng, M. Hatzistergos, P. Y. Hung, R. Tieckelmann, W. Tsai, C. Hobbs and P. D. Ye, *presented in part at the 2014 Symposium on VLSI Technology (VLSI-Technology): Digest of Technical Papers*, 9-12 June 2014.
186 D. Kiriya, M. Tosun, P. Zhao, J. S. Kang and A. Javey, *J. Am. Chem. Soc.*, 2014, **136**, 7853–7856.
187 Y. Shi, J.-K. Huang, L. Jin, Y.-T. Hsu, S. F. Yu, L.-J. Li and H. Y. Yang, *Sci. Rep.*, 2013, **3**, 1839.
188 M. S. Choi, D. Qu, D. Lee, X. Liu, K. Watanabe, T. Taniguchi and W. J. Yoo, *ACS Nano*, 2014, **8**, 9332–9340.
189 S. I. Khondaker and M. R. Islam, *J. Phys. Chem. C*, 2016, **120**, 13801–13806.
190 M. Chen, H. Nam, S. Wi, L. Ji, X. Ren, L. Bian, S. Lu and X. Liang, *Appl. Phys. Lett.*, 2013, **103**, 142110.
191 W.-M. Kang, S. Lee, I.-T. Cho, T. H. Park, H. Shin, C. S. Hwang, C. Lee, B.-G. Park and J.-H. Lee, *Solid-State Electron.*, 2018, **140**, 2–7.
192 F. Giannazzo, G. Fisichella, G. Greco, S. Di Franco, I. Deretzis, A. La Magna, C. Bongiorno, G. Nicotra, C. Spinella, M. Scopelliti, B. Pignataro, S. Agnello and F. Roccaforte, *ACS Appl. Mater. Interfaces*, 2017, **9**, 23164–23174.
193 N. Haiyan, W. Zhangting, J. Jie, Z. Amina, Y. Yumeng and N. Zhenhua, *J. Phys. D: Appl. Phys.*, 2017, **50**, 154001.
194 B. J. Lee, B. J. Lee, J. Lee, J.-W. Yang and K.-H. Kwon, *Thin Solid Films*, 2017, **637**, 32–36.
195 J. Guo, B. Yang, Z. Zheng and J. Jiang, *Phys. E*, 2017, **87**, 150–154.
196 C. P. Lin, C. T. Lin, P. S. Liu, M. J. Yu and T. H. Hou, *presented in part at the 2016 IEEE 16th International Conference on Nanotechnology (IEEE-NANO)*, 22-25 Aug. 2016.
197 M. Tosun, L. Chan, M. Amani, T. Roy, G. H. Ahn, P. Taheri, C. Carraro, J. W. Ager, R. Maboudian and A. Javey, *ACS Nano*, 2016, **10**, 6853–6860.
198 H. Yang, S. W. Kim, M. Chhowalla and Y. H. Lee, *Nat. Phys.*, 2017, **13**, 931.
199 X. Qian, J. Liu, L. Fu and J. Li, *Science*, 2014, **346**, 1344–1347.
200 P. Li, Y. Wen, X. He, Q. Zhang, C. Xia, Z.-M. Yu, S. A. Yang, Z. Zhu, H. N. Alshareef and X.-X. Zhang, *Nat. Commun.*, 2017, **8**, 2150.
201 J. Zhu, Z. Wang, H. Yu, N. Li, J. Zhang, J. Meng, M. Liao, J. Zhao, X. Lu, L. Du, R. Yang, D. Shi, Y. Jiang and G. Zhang, *J. Am. Chem. Soc.*, 2017, **139**, 10216–10219.
202 B. Ouyang, S. Xiong and Y. Jing, *NPJ 2D Mater. Appl.*, 2018, **2**, 13.
203 S. Cho, S. Kim, J. H. Kim, J. Zhao, J. Seok, D. H. Keum, J. Baik, D.-H. Choe, K. J. Chang, K. Suenaga, S. W. Kim, Y. H. Lee and H. Yang, *Science*, 2015, **349**, 625–628.
204 Y.-C. Lin, D. O. Dumcenco, Y.-S. Huang and K. Suenaga, *Nat. Nanotechnol.*, 2014, **9**, 391.
205 Y. Yu, G.-H. Nam, Q. He, X.-J. Wu, K. Zhang, Z. Yang, J. Chen, Q. Ma, M. Zhao, Z. Liu, F.-R. Ran, X. Wang, H. Li, X. Huang, B. Li, Q. Xiong, Q. Zhang, Z. Liu, L. Gu, Y. Du, W. Huang and H. Zhang, *Nat. Chem.*, 2018, **10**, 638–643.
206 Y. Ma, B. Liu, A. Zhang, L. Chen, M. Fathi, C. Shen, A. N. Abbas, M. Ge, M. Mecklenburg and C. Zhou, *ACS Nano*, 2015, **9**, 7383–7391.
207 D. Marian, E. Dib, T. Cusati, A. Fortunelli, G. Iannaccone and G. Fiori, *presented in part at the 2016 IEEE International Electron Devices Meeting (IEDM)*, 3-7 Dec. 2016.
208 K. Kang, S. Xie, L. Huang, Y. Han, P. Y. Huang, K. F. Mak, C.-J. Kim, D. Muller and J. Park, *Nature*, 2015, **520**, 656.
209 K. Kang, K.-H. Lee, Y. Han, H. Gao, S. Xie, D. A. Muller and J. Park, *Nature*, 2017, **550**, 229.
210 X. Zhang, Z. Lai, C. Tan and H. Zhang, *Angew. Chem., Int. Ed.*, 2016, **55**, 8816–8838.
211 C. Tan and H. Zhang, *Chem. Soc. Rev.*, 2015, **44**, 2713–2731.
212 D. J. Groenendijk, M. Buscema, G. A. Steele, S. Michaelis de Vasconcellos, R. Bratschitsch, H. S. van der Zant and A. Castellanos-Gomez, *Nano Lett.*, 2014, **14**, 5846–5852.
213 J. Guo, J. Jiang, Z. Zheng and B. Yang, *Org. Electron.*, 2017, **40**, 75–78.
214 D. H. Kang, M. S. Kim, J. Shim, J. Jeon, H. Y. Park, W. S. Jung, H. Y. Yu, C. H. Pang, S. Lee and J. H. Park, *Adv. Funct. Mater.*, 2015, **25**, 4219–4227.
215 H. Fang, M. Tosun, G. Seol, T. C. Chang, K. Takei, J. Guo and A. Javey, *Nano Lett.*, 2013, **13**, 1991–1995.